1   **Where does the dust deposited over the Sierra Nevada snow come from?**

2

3   Huilin Huang[1*], Yun Qian[1*], Ye Liu[1], Cenlin He[2], Jianyu Zheng[3,4], Zhibo Zhang[3,4], Antonis Gkikas[5]

4

5   [1]Atmospheric Sciences and Global Change Division, Pacific Northwest National Laboratory, Richland, WA,

6   USA

7   [2]Research Applications Laboratory, National Center for Atmospheric Research, Boulder, CO, USA

8   [3]Department of Physics, University of Maryland Baltimore County, Baltimore, MD, USA

9   [4]Joint Center for Earth Systems Technology, University of Maryland Baltimore County, Baltimore, MD, USA

10   [5]Institute for Astronomy, Astrophysics, Space Applications and Remote Sensing, National Observatory of

11   Athens, Athens, Greece

12

13   *Corresponding to: Huilin Huang, Huilin.huang@pnnl.gov; Yun Qian, Yun.Qian@pnnl.gov

14

15

16

17   Submitted to Atmospheric Chemistry and Physics

18

Abstract

Mineral dust contributes up to one-half of surface aerosol loading in spring over the southwestern U.S., posing an environmental challenge that threatens human health and the ecosystem. Using the self-organizing map (SOM) analysis with dust deposition and fluxes data from WRF-Chem and Modern-Era Retrospective analysis for Research and Applications, Version 2 (MERRA-2), we identify four typical dust transport patterns across the Sierra Nevada, associated with the mesoscale winds, Sierra-Barrier-Jets (SBJ), North-Pacific-High (NPH), and long-range cross-Pacific westerlies, respectively. We find that dust emitted from the Central Valley is persistently transported eastward, while dust from the Mojave Desert and Great Basin influences the Sierra Nevada during mesoscale transport occurring mostly in winter and early spring. Asian dust reaching the mountain range comes either from the west through straight isobars (cross-Pacific transport) or from the north in the presence of the NPH. Extensive dust depositions are found on the west slope of the mountain, contributed by Central Valley emissions and cross-Pacific remote transport. Especially, the SBJ-related transport produces deposition through landfalling atmospheric rivers, whose frequency might increase in a warming climate.

1. Introduction

The emission, transport, and deposition of mineral dust (hereafter dust) are processes receiving increasing interest from the scientific community (Sarangi et al., 2020). Dust emission is an integral part of aridification and mirrors the effects of climatic change and anthropogenic land use on global drylands (Duniway et al., 2019). Airborne dust interacts with Earth's climate system by altering the radiation budget and cloud lifetime and amount (Forster et al., 2007; Haywood et al., 2005; Huang et al., 2019; Liu et al., 2022b). Research has indicated that exposure to dust particles can cause respiratory infections, heart disease, and chronic obstructive pulmonary disease (COPD) (Laden et al., 2006; Lim et al., 2012; Crooks et al., 2016). A significant association between dust exposure and increased mortality has been reported, but there is no consensus in this regard to date (Giannadaki et al., 2014). The deposition of dust on snow surface influences snow albedo, further contributing to anthropogenic climate change as early as the 1970s (Qian et al., 2009; Qian et al., 2014; Skiles et al., 2018).

Dust over the southwestern U.S., particularly in California and Nevada states, is an important aerosol type contributing to more than half of surface aerosol concentrations in spring (Kim et al., 2021). Covered by dry soil with large gaps and sparse vegetation, the surrounding Mojave Desert, Sonoran Desert, and Great basin are susceptible to wind erosion (Okin et al., 2006; Duniway et al., 2019). The dry or ephemeral lakes in the deserts produce very fine dust containing toxic inorganic constituents (Goldstein et al., 2017). In addition, anthropogenic land-use practices – e.g., agriculture and human settlement, have greatly disturbed crustal biomass and produced windblown dust along the west coast (Pappagianis and Einstein, 1978; Clausnitzer and Singer, 2000; Neff et al., 2008). Furthermore, cross-Pacific dust transported from Asia and Africa to the Sierra Nevada range is widely reported (Ault et al., 2011; Creamean et al., 2014; Creamean et al., 2013). The surface dust concentration has been found to increase in the past two decades during spring at sites across the Southwest (Tong et al., 2017; Hand et al., 2017; Brahney et al., 2013), and the onset of dust season is shifting earlier in response to climate change (Hand et al., 2016). The elevated dust emission and earlier dust season are supposed to lead to a spectrum of environmental and societal

58   impacts in the most populated U.S. state. Especially, the resultant dust deposition on mountain snow

59   decreases snow albedo and produces a radiation forcing of 0-14.6 W m^{-2} during the melting season (Huang

60   et al., 2022a), shifting snowmelt timing to earlier dates and further increasing California's vulnerability to

61   water resource fluctuations (Wu et al., 2018; Huang et al., 2022b). With its complex terrains, frequently

62   varying microclimate, and coexisting sources from both local and remote regions, the Sierra Nevada area

63   is an interesting region for studying dust transport and its response to climate change.

64   Characterization of dust emission, transport, and deposition across the Sierra Nevada has been

65   investigated using various data. Isotopic analyses (i.e., concentrations of Pb, Nd) are widely used to

66   distinguish and quantify the respective contribution of dust emission from local (dried Owen Lakes),

67   regional (Central Valley and the Mojave Desert), and global sources (Asia and Africa) on the dust

68   deposition on the mountain (Muhs et al., 2007; Jardine et al., 2021; Aciego et al., 2017; Aarons et al., 2019).

69   Their source attribution has been generally confirmed by the analyses of dust particle size and composition

70   (Creamean et al., 2014; Creamean et al., 2013; Reheis and Kihl, 1995). The isotopic and composition

71   analyses have been commonly used with back-trajectory modeling to further identify the dust transport

72   pathway from the source to the deposition location (Vicars and Sickman, 2011; Creamean et al., 2014;

73   Creamean et al., 2013). Yet, these analyses generally retrieve dust sources in a short time and at a specific

74   location. Alternatively, ground-based measurement networks were established in the 1990s and provide

75   long-term trends of dust concentrations and the interannual variability across multiple sites (Hand et al.,

76   2017; Achakulwisut et al., 2017; Hand et al., 2016). However, they do not contain information on dust

77   origins and atmospheric conditions responsible for dust transport. Satellite retrievals were less commonly

78   used to study dust characteristics across the Sierra Nevada (Lei and Wang, 2014), mainly due to the poor

79   data coverage caused by cloud contamination in the region.

80   Global and regional climate-chemistry models have been widely used to understand the drives of

81   the variability of dust and quantify the role of regional and remote transport, filling the gaps in the

82   observations (Chin et al., 2002; Chin et al., 2007; Kim et al., 2021; Wu et al., 2017). While dust emissions

83   and transport have been generally studied, there lacks a connection between dust emissions from the source

84 region and the timing, location, and amount of dust deposition to the Sierra Nevada snow. The isotopic and

85 composition analyses attribute dust sources at a few sites. But to our knowledge, no regional

86 characterization has been conducted on how dust is transported to the Sierra Nevada after emissions from

87 adjacent drylands and remote continents and when, where, and how much depositions occur for dust

88 transported through different pathways. The connection between dust emissions, transport pathways, and

89 deposition to snow would facilitate the prediction of future changes in dust regimes and the corresponding

90 climate impact, enabling more efficient management practices. With a focus on the dust that influences the

91 Sierra Nevada, this study investigates 1) Where does the dust come from? 2) How is dust transported to the

92 mountain from the sources? 3) How is the dust deposited on the Sierra Nevada during spring, when the

93 dust-in-snow largely influences snow albedo and snowmelt? We integrate models and observations to

94 understand how the dust deposition is linked to a specific source both surrounding and far from the Sierra

95 Nevada.

96

97 **2.1 Model and Reanalysis datasets**

98 **2.1.1 WRF-Chem configuration**

99 Table 1. Model configuration.

Atmospheric processes	WRF-Chem Configuration
Meteorological IC/LBCs	ERA5
Microphysics	Morrison double-moment
Radiation	RRTMG for both shortwave/longwave
Land surface	CLM4 with SNICAR
Surface layer	Revised MM5 Monin-Obukhov
Planetary boundary layer	YSU scheme
Cumulus	Grell-Freitas
Chemical driver	MOZART
Aerosol driver	MOSAIC 4-bin
Anthropogenic emission	NEI2017
Biogenic emission	MEGAN
Biomass burning emission	FINNv2.2

Dust emission	GOCART
Chemical IC/BC conditions	CAM-Chem

100
101   We used the WRF-Chem version 3.9 to study dust emission and transport across the Sierra Nevada.

102   The model setups (Table 1), including the physical schemes and emission inventory, follow Huang et al.

103   (2022a), which showed that the model captures the distribution and variation in aerosols reasonably well in

104   the study domain (126.12-112.86°W, 32.3-43.0°N). The Model of Ozone and Related chemical Tracers

105   (MOZART) chemistry module (Emmons et al., 2020) and the Model for Simulating Aerosol Interactions

106   and Chemistry with four bins (MOSAIC 4-bin) aerosol model (Zaveri and Peters, 1999) were applied, and

107   dust emissions were calculated "online" using the GOCART dust scheme (Ginoux et al., 2001). The

108   meteorological initial and lateral boundary conditions were derived from the ECMWF Reanalysis v5

109   (ERA5) at 0.25° horizontal resolution and 6 h temporal intervals (Hersbach et al., 2020). Spectral nudging

110   was employed with a timescale of 6 h above the PBL to reduce the drift between ERA5 reanalysis data and

111   WRF's internal tendencies (Von Storch et al., 2000). The chemical initial and boundary conditions were

112   provided by CAM-Chem (Buchholz et al., 2019).

113   We applied the model to two nested domains (Fig. 1). Domain 1 (126.12-112.86°W, 32.3-43.0°N)

114   was configured to cover all of California, Nevada, and part of the surrounding states with 110×120 grid

115   cells at 10 km $\times$ 10 km horizontal resolution; the nested domain 2 covered the Sierra Nevada and

116   surrounding regions with a 2 km $\times$ 2 km resolution. The cumulus scheme is turned off in domain 2 with

117   convection-permitting resolution. We used 35 vertical model layers from the surface to 10 hPa with denser

118   layers at lower altitudes to resolve the PBL. The simulation period ranged from September 20, 2018, to

119   August 31, 2019 while we only used output from February to June in consideration of both dust emission

120   season and mountain snow existence (Hand et al., 2016; Kim et al., 2021; Achakulwisut et al., 2017).
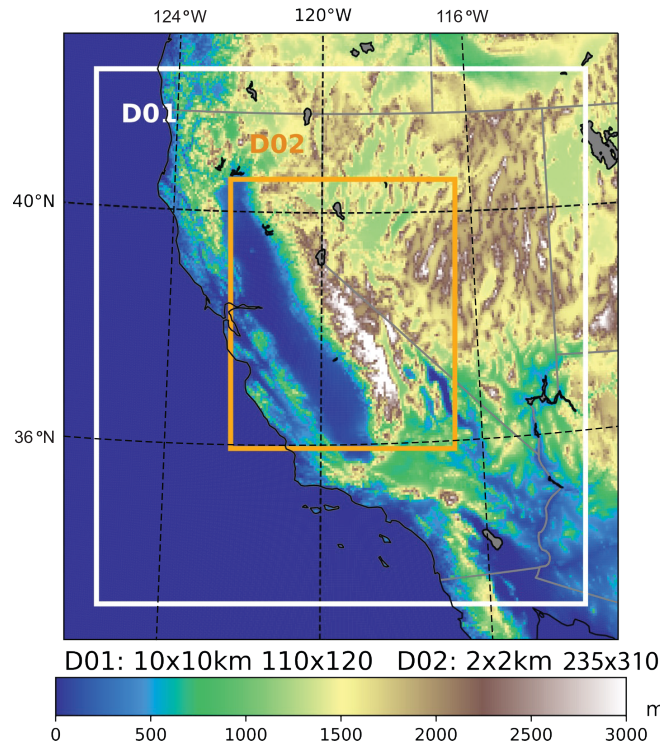
Figure 1 WRF-Chem simulation domain 1 (D01) and domain 2 (D02) used in this study

2.1.2 MERRA-2 and ERA5 reanalysis

The Modern-Era Retrospective analysis for Research and Applications, Version 2 (MERRA-2) is a widely used atmospheric reanalysis with a spatial resolution of $0.500° \times 0.625°$ and 72 vertical layers (Buchard et al., 2017). MERRA-2 aerosol products are produced by combining GEOS atmospheric model version 5 (GEOS-5) with a 3D variational data assimilation algorithm to incorporate satellite observations, including Advanced Very High Resolution Radiometer (AVHRR), Moderate Resolution Imaging Spectroradiometer (MODIS), and Multi-angle Imaging Spectro Radiometer (MISR), as well as ground-based observations such as the AEronet RObotic NETwork (AERONET) (Gelaro et al., 2017). Although the aerosol vertical profile, composition, and size distributions are not constrained by the assimilation of aerosol optical depth (AOD), previous studies demonstrated that the aerosol assimilation system has considerably improved the agreement with numerous observed aerosol properties (Buchard et al., 2016; Buchard et al., 2017; Randles et al., 2017). The assimilation results in the imbalance of global dust mass and produces a considerably larger deposition than the simulated dust emission (Buchard et al., 2017).

137 MERRA-2 simulates dust with diameter bins of 0.2–2.0 (DU001), 2.0–3.6 (DU002), 3.6–6.0 (DU003), 6.0–

138 12.0 (DU004), and 12.0–20.0 (DU005) μm, while the MOSAIC 4-bin in WRF-Chem simulates dust with

139 geometric size bins of 0.039–0.156, 0.156–0.625, 0.625–2.5, and 2.5–10.0 μm. We therefore use the dust

140 concentrations of the first 4 size bins in MERRA-2 (DU001 + DU002 + DU003 + 0.74 * DU004) to match

141 with dust with geometric size less than 10.0 μm in WRF-Chem

142 (https://gmao.gsfc.nasa.gov/reanalysis/MERRA-2/FAQ/).

143 ERA5 provides assimilated wind fields at a 0.25°×0.25° horizontal resolution at 137 hybrid

144 sigma/pressure levels from 1979 to near real time (Hersbach et al., 2020). This study obtained the 3-hourly

145 meridional and zonal wind field from February to June 2019 from 1000 to 500 hPa. The ERA5 wind

146 reanalyses were used with satellite-retrieved dust optical depth (DOD) to evaluate the classified dust

147 emission and transport patterns from the model.

148

149 **2.2 Satellite observations for validation**

150 The Infrared Atmospheric Sounding Interferometer (IASI) onboarded European Meteorological

151 Operation (MetOp) satellite series measures infrared radiation in 8,461 spectral channels between 3.63 and

152 15.5 μm. The instrument has provided near-global coverage with a spatial resolution of 12 km at nadir

153 (Hilton et al., 2012) since 2007. IASI is primarily sensitive to coarse-mode dust particles, and thus the

154 retrieved AOD at the wavelength of 10 μm can represent the DOD (Yu et al., 2019). Note that the thermal

155 infrared (IR) AOD reported by IASI is usually significantly smaller than the visible AOD in MODIS,

156 because of the spectral dependence of dust extinction (Zheng et al., 2022). We use the version 2.2 AOD

157 product developed at the Centre National de la Recherche Scientifique Laboratoire de Météorologie

158 Dynamique from https://iasi.aeris-data.fr/dust-aod/ (February 2022) (Capelle et al., 2014). The 0.3°×0.3°

159 daily AOD data covering California were produced by aggregating day and night retrievals at the satellite

160 pixel resolution (Capelle et al., 2018), in consideration of both data completeness and fine features. The

161 1.0°×1.0° daily AOD was produced in a similar way to investigate dust transport from Asia across the North

162 Pacific.

163   The MIDAS (ModIs Dust AeroSol) dataset provides global fine-resolution (0.1°×0.1°) daily DOD

164   between 2003 and 2017 using quality-filtered AOD from MODIS Aqua and DOD-to-AOD ratios from

165   MERRA-2 reanalyses (Gkikas et al., 2021). Despite the uncertainties in modeled DOD-to-AOD ratios, the

166   validations of the MIDAS dataset against the AERONET dust-like AOD and the LIdar climatology of

167   Vertical Aerosol Structure for space-based lidar simulation (LIVAS) DOD reveal a high level of agreement

168   at both global and station level (Gkikas et al., 2022). Compared with other MODIS-derived DOD products

169   (Song et al., 2021; Voss and Evan, 2020; Ginoux et al., 2012; Pu and Ginoux, 2018), MIDAS has finer

170   spatial and temporal resolutions over both land and ocean, which is particularly applicable in this study

171   focusing on a small region and a few cases at daily scale. The dataset has been extended to near real-time

172   to match our study year.

173   Cloud-Aerosol Lidar with Orthogonal Polarization (CALIOP) is a two-wavelength (532 and 1064

174   nm) polarization lidar onboarded the Cloud-Aerosol Lidar and Infrared Pathfinder Satellite Observation

175   (CALIPSO) satellite (Hunt et al., 2009). Since June 2006, the lidar has been collecting an almost continuous

176   record of high-resolution profiles of aerosol and clouds as fine as 30 m in the vertical, covering 82°N to

177   82°S (Winker et al., 2010; Winker et al., 2009). This study used clear-sky data from the CALIOP Version

178   4, level-2 aerosol profile product (Young et al., 2018) to investigate the vertical profile of elevated dust

179   layer, especially from remote transport. When there were large DOD shown in IASI and MIDAS, we

180   examined the vertical profiles of dust by identifying the "dust," "polluted dust," and "dusty marine" species

181   in the CALIOP data (Kim et al., 2018)

182

183   **2.3 SOM analysis**

184   We applied the self-organizing map (SOM), a clustering method developed in the field of artificial

185   neural networks, to recognize different weather features associated with dust transport and deposition..

186   SOM has been widely used in atmospheric sciences to recognize spatially organized sets of patterns in the

187   data (Reusch et al., 2007; Bao and Wallace, 2015; Liu et al., 2022a; Song et al., 2019). Before the machine-

188   learning process, Before the machine learning process, we assign a few two-dimensional arrays of initial

189   nodes randomly or more efficiently from the leading empirical orthogonal functions (EOFs). During the

190   training phase, the Euclidean distance between each input pattern and the initiation nodes is calculated to

191   begin an iterative procedure. The best-matching node or the "winning" node is the one with the smallest

192   distance between the initiation nodes and the input vector. Then the winning node and the neighborhood

193   nodes around the winner are updated to adjust themselves toward the input vector. Since this process is

194   iterated and fine-tuned, the nodes are self-organizing. The final SOM nodes represent typical dust transport

195   and deposition patterns across the Sierra Nevada.

196   Here, we first used five variables from WRF-Chem inner domain (D02) in the SOM clustering,

197   including dust deposition flux at the Sierra Nevada, the low-level meridional and zonal dust transport fluxes,

198   and the mid-level meridional and zonal dust transport fluxes surrounding the Sierra Nevada. The original

199   fields were used without any no filtering methods to consider the extreme cases. The 3 hourly model outputs

200   during February-June 2019 are used to count for the spatial distribution and temporal evolution of dust

201   transport and deposition. For WRF-Chem, we averaged the zonal and meridional dust fluxes in model levels

202   3-5 (roughly 900-950 hPa over coastal California and 650-700 hPa over the Sierra Nevada) to acquire the

203   low-level transport features. We averaged 200-700 hPa fluxes to acquire the mid-level transport features.

204   Levels 3-5 were selected to focus on airborne particulate matter entrained above the planetary boundary

205   layer and transported on the regional scale. Remote transport of Asian and African dust is mostly found

206   around 600–200 hPa, which flows downward to the lower troposphere along the post-cold isentropic surface

207   into the atmospheric river (AR) environment (Voss et al., 2021). By selecting levels between 200-700 hPa,

208   we were able to include all cross-Pacific remote transport in the middle level.

209   We tested the number of clusters (k) that ranges in 3, 4, 5, 6, 8, 9, and 16 to assess the distinctiveness

210   and robustness of different k. For each k, the robustness of the clusters was measured by a classifiability

211   index (CI) (Vigaud and Robertson, 2017; Vigaud et al., 2018; Hannachi, 2010) constructed using the

212   minimum spatial correlation coefficient between the clusters obtained from the full data and many random

213   halves of the data (100 halves used here) (Hannachi, 2010). Therefore, the CI measured the reproductivity

214   of the k clusters partitioning (Visbeck et al., 2001), with perfect partitioning leading to 1. Figure S1 shows

215 the CI as a function of the number of clusters using WRF-Chem output for 2019. With the highest CI, the

216 4-cluster partitioning well represents distinct dust transport and deposition patterns over the Sierra Nevada

217 and is used in this study.

218   To verify the recognized transport patterns based on WRF-Chem, we conducted SOM analyses

219 using variables from MERRA-2. We first remapped the same five variables using bilinear interpolation

220 from $0.5° \times 0.625°$ to 10 km, the resolution of the WRF-Chem outer domain, before clustering. The vertical

221 levels of low-level and mid-level dust transport fluxes were selected to approximately match the WRF-

222 Chem pressure level. Four nodes were identified and arranged to make a direct comparison with those from

223 WRF-Chem. To further investigate if transport patterns recognized from SOM vary significantly with years,

224 we applied SOM analyses over 2001-2021 using MERRA-2 extended records of dust fluxes and deposition.

225

226 **3. Results**

227 **3.1 Dust emission sources around the Sierra Nevada**

228   We find four emission source regions surrounding the Sierra Nevada where dust emissions could

229 potentially influence the mountain snow impurities between February and June (Fig. 2). The Mojave Desert,

230 located southeast of the Sierra Nevada, is characterized by low annual precipitation, sparse vegetation, and

231 dried fine soil. Airborne dust loading over the desert can reach 30000 ug m^{-2} averaged over our study period

232 (Fig. 2a). It is generally transported eastward but can also be transported westward, influencing the southern

233 part of the mountain (Neff et al., 2008). Dust produced in the northern (Sacramento Valley) and the southern

234 part (San Joaquin and Tulare Basins) of the Central Valley is often transported eastward to the mountains.

235 With high soil aridity and a higher fraction of dry sand (Duniway et al., 2019), the southern Central Valley

236 is more erodible and emits a higher amount of fine dust. The Great Basin dust is relatively weak in

237 magnitude but located at a higher altitude. Therefore, it can easily ride along wind currents upward along

238 the east slope of the mountain. The column dust loading in MERRA-2 confirms our results in WRF-Chem

239 (Fig. 2b), despite it showing a stronger dust emission in the Great Basin while a weaker one in the

240 Sacramento Valley. The IASI shows the strongest IR DOD in the Mojave Desert, followed by the southern

241 Central Valley, but smaller dust emissions from the Sacramento Valley as compared with model output

242 (Fig. 2c). The smaller magnitude is largely due to the fact that IASI measures the radiation at IR

243 wavelengths, which is more sensitive to coarse-mode dust particles (Yu et al., 2019), whereas the fine dust

244 produced in the Central Valley has a negligible contribution to DOD at 10 μm. In contrast, MIDAS captures

245 dust emissions from the Great Basin, the southern and northern Central Valley (Fig. 2d) but not the Mojave

246 Desert. MIDAS is reported to underestimate DOD from the Mojave Desert compared to AERONET DOD,

247 which might be caused by the lower dust amounts simulated in MERRA-2 (Gkikas et al., 2021) and the

248 underestimation of MODIS AOD over the deserts as compared to ground observations (Tao et al., 2017).
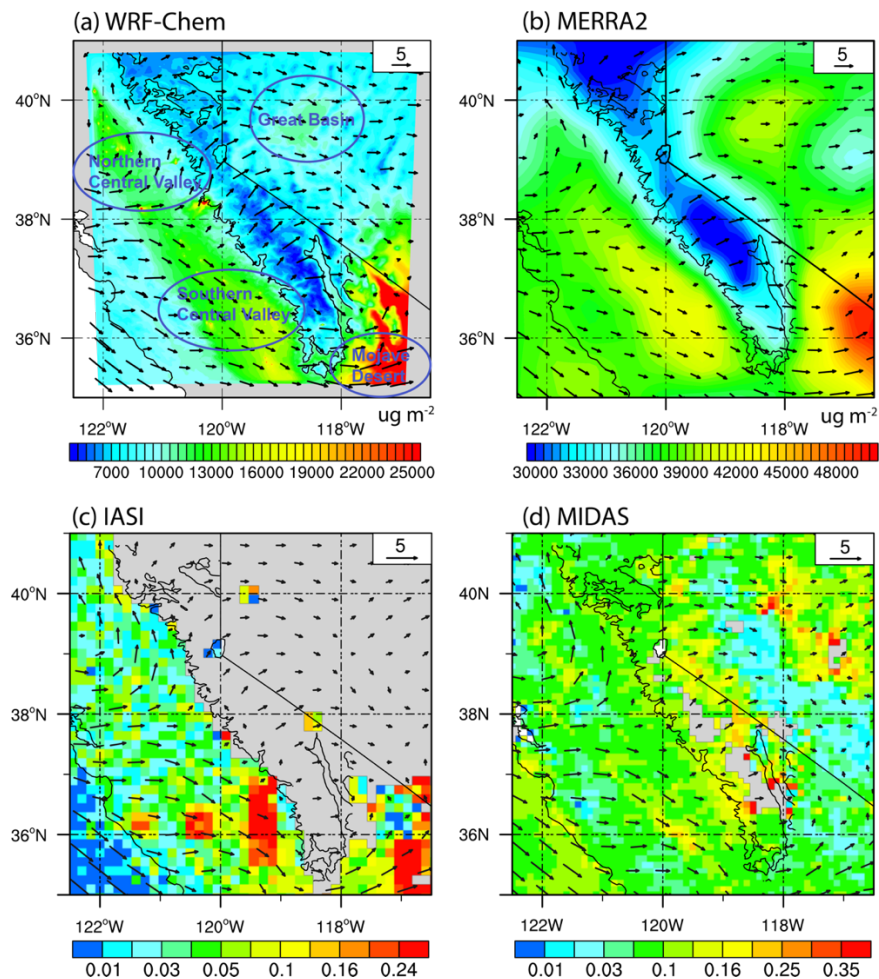
249
250 **Figure 2** The spatial distribution of dust in model and satellite observations averaged in 2019 February-
251 June. Column dust loading (ug m^{-2}) and low-level winds (roughly 875-925 hPa; m s^{-1}) in (a) WRF-Chem
252 and (b) MERRA-2. (c) Observed thermal infrared DOD at the wavelength of 10 μm from IASI (d) Observed
253 visible DOD at the wavelength of 550 μm from MIDAS. The low-level winds (m s^{-1}) in (c) and (d) are from
254 ERA5 reanalyses. Black contours indicate anthe elevation of 1500 m, which represents the Sierra Nevada
255 range used in this study. The grey area in c-d are missing pixels in satellite observations

12

256

3.2 Dust transport across the Sierra Nevada
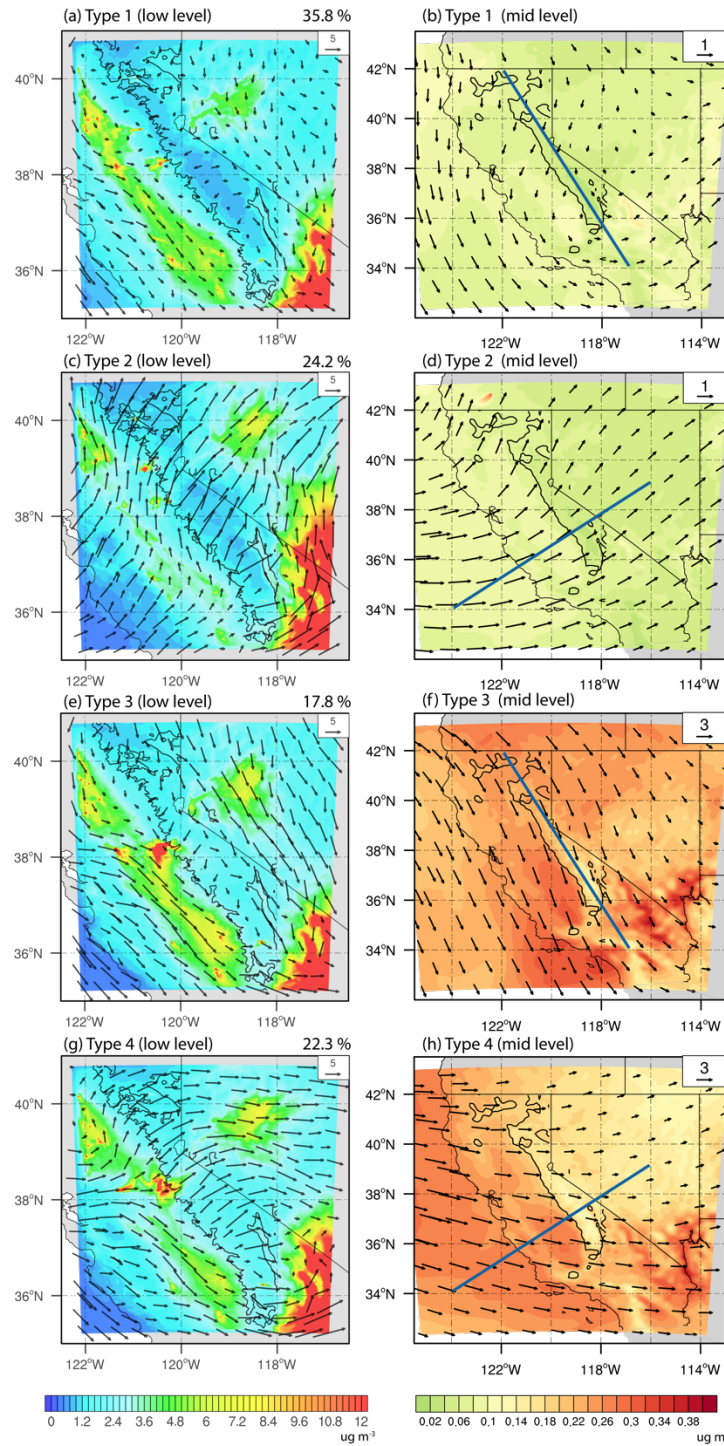
258
Figure 3 (a, c, e, g) Low-level (roughly 875-925 hPa) dust concentration (ug m^{-3}) and wind vectors (m s^{-1})
in each of the four SOM type in WRF-Chem; The numbers on the top right of subplots denote the frequency
of each type. (b, d, f, h) Mid-level (200-700 hPa average) dust concentration (ug m^{-3}) and dust transport in
types 1-4; The position of the cross-section used for Figure 5 is denoted in each plot.

263

This section introduces the features of dust transport patterns discerned from WRF-Chem and evaluates them against satellite observations over the period of February to June 2019. Figure 3 shows the WRF-Chem dust concentration and wind in the low levels and middle levels averaged for each of the four types acquired from the SOM analyses. The dust transport pattern represented in SOM type 1 accounts for 35.8% of hours from February to June (Fig. 3a), especially in February (43%) and March (57%) (Fig. 4a). Type 2 occurs in 24.2% of the whole study period and contributes to more than 50% in February and then decreases with the month. In contrast, types 3 and 4 account for 17.8% and 22.3%, respectively, with the occurrence increasing with the month. The maximum occurrence is found in June for type 3 (40%) and April for type 4 (34%), respectively.

3.2.1 Mesoscale regional (MSR) transport
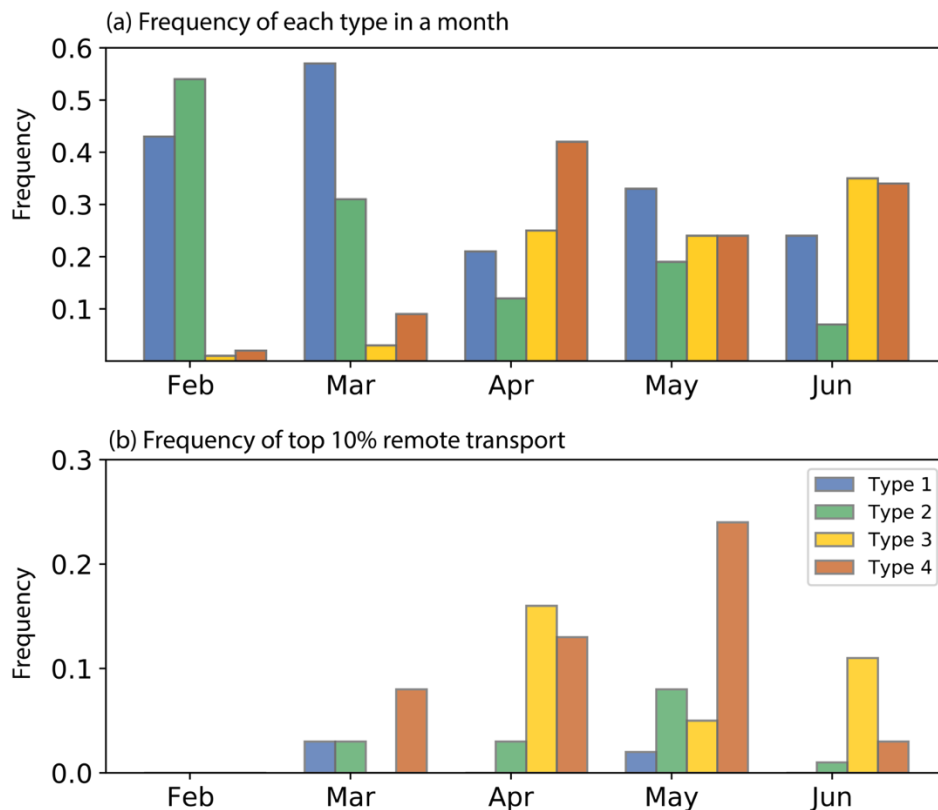
Figure 4 (a) The frequency of each type (the time dominated by each type divided by total time in a month) that occurs in February, March, April, May, and June in WRF-Chem. (b) The frequency of each type in the top 10% remote transport (the time dominated by each type divided by the total time of the top 10% remote transport).

279

280   In type 1, dust is transported from northwest to southeast in the Central Valley in the low level

281   (roughly 875-925 hPa over the California coast). A vortex (Schultz Eddy) was found in the northern Central

282   Valley (Fig. 3a), circulating counter-clockwise and confining dust to the local environment (Bao et al.,

283   2008). The air inflow from the ocean is relatively weak and obstructed by the terrain. The Great Basin is

284   dominated by the northwesterlies. The emitted dust is transported southeastward and blocked by the

285   mountain, depositing dust on the east slope. Dust emitted from the Mojave Desert can be elevated to the

286   middle level (Fig. 3b). The cross-section further shows a vertical circulation where the Mojave Desert dust

287   is blown away from the Sierra Nevada at the low level and towards the mountain at 600-700 hPa (Fig. 5a).

288   A weaker mid-level cross-Pacific flow is found in type 1 than in other types (Fig. 6a), with no signals of

289   remote transport reaching the Sierra Nevada (Fig. 3b). Type 1 generally corresponds to the dust transport

290   in lack of prevailing large-scale weather systems. The high peaks of the Sierra Nevada produce mesoscale

291   circulations and prevent the Central Valley and Great Basin dust from being transported to the other side

292   of the mountain. It is referred to as the "mesoscale regional (MSR) transport" hereafter.
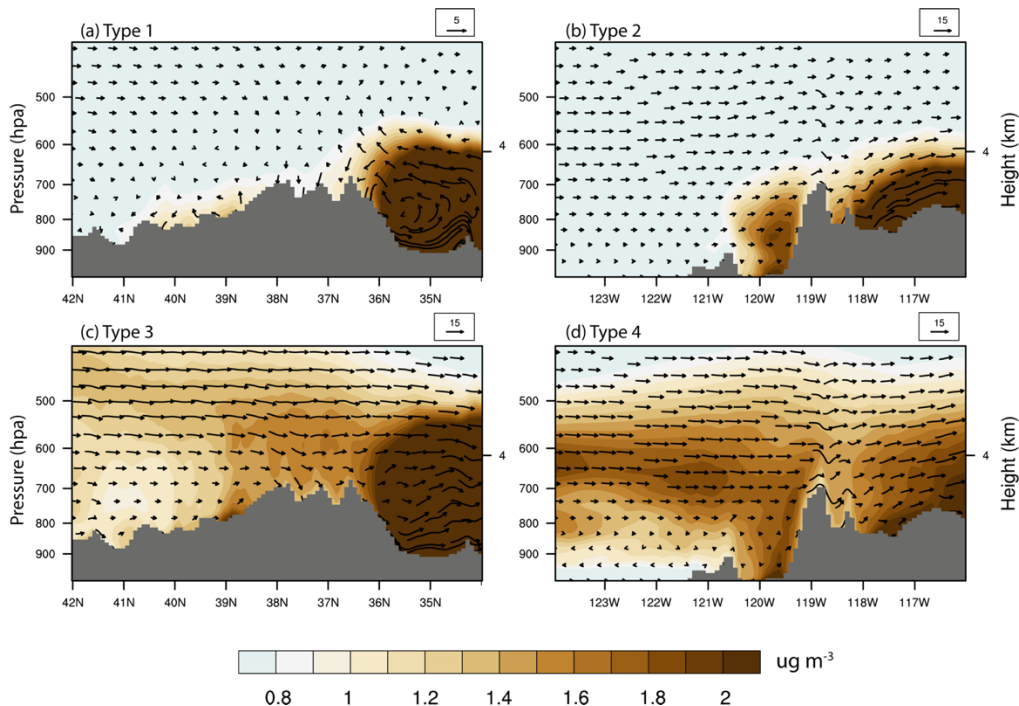

293
294   **Figure 5** Cross-section of dust concentration (shaded; ug m^{-3}) and dust transport fluxes (vectors; ug m^{-2} s^{-1}
295   ^{1}) at 1000-400 hPa for each SOM type in WRF-Chem. The position of each cross-section is denoted in Fig.
296   3 b (Type 1), d (Type 2), f (Type 3), and h (Type 4). The grey area indicates the topography of the Sierra
297   Nevada.
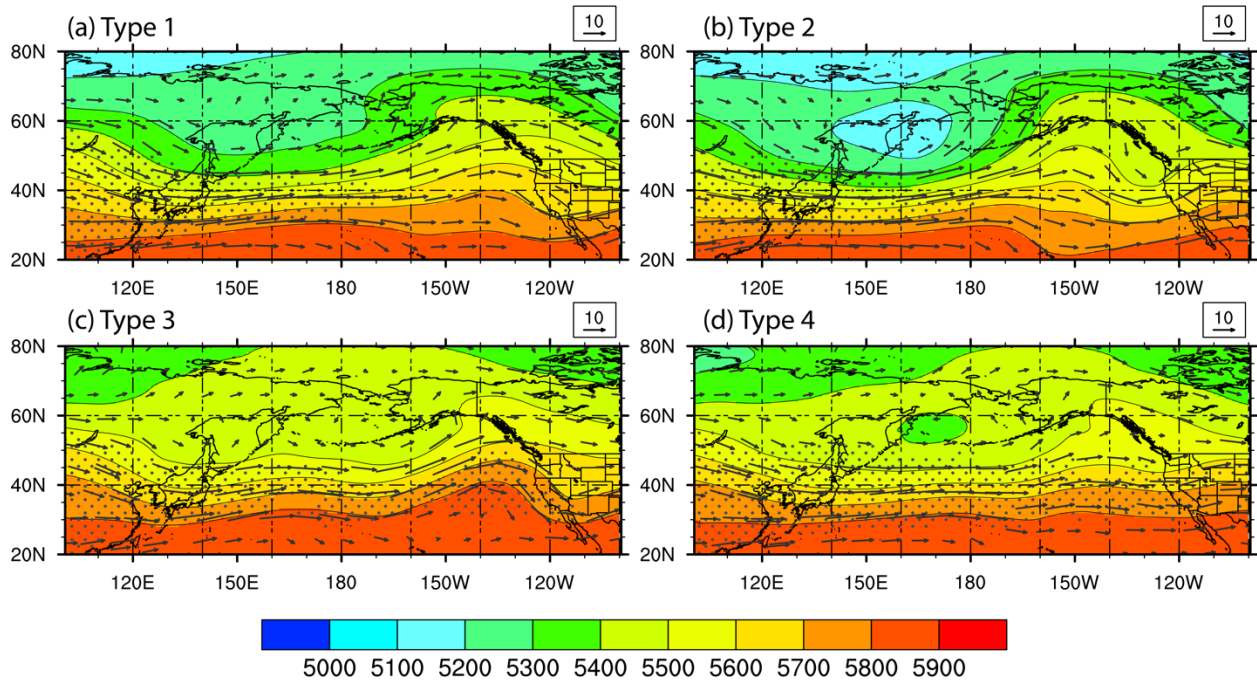
Figure 6 Geopotential height (gpm) and wind vectors (m s^{-1}) at 500 hPa in each of the four SOM types in WRF-Chem. The dotted regions indicate DOD higher than 0.03 from MERRA-2

We validate the features of type 1 from WRF-Chem using satellite-–retrieved DOD and wind vectors from ERA5. The cloud contamination results in many missing satellite pixels in our study domain, making the transport patterns hard to discern on a single day. DOD and winds belonging to the same SOM type on consecutive days are averaged to maximize the data completeness. One typical example for each type is presented based on their representativeness and the maximum spatial coverage. Figures 7a-b present dust emission and transport patterns during May 10-12, a typical case for the MSR transport. In IASI, we find peak IR DOD (> 0.2) over the Mojave Desert and the southern Central Valley and moderate values in the Sacramento Basin related to the Schultz Eddy (Fig. 5a), resembling the relative magnitude of dust concentrations in regional source regions in WRF-Chem (Fig. 3a). MIDAS shows another evidence of dust transport pathways within the Central Valley with a higher resolution, although the maximum DOD shifts slightly towards the mountain range (Fig. 7b). Dust emissions from the Great Basin are weaker than those from the southern Central Valley.
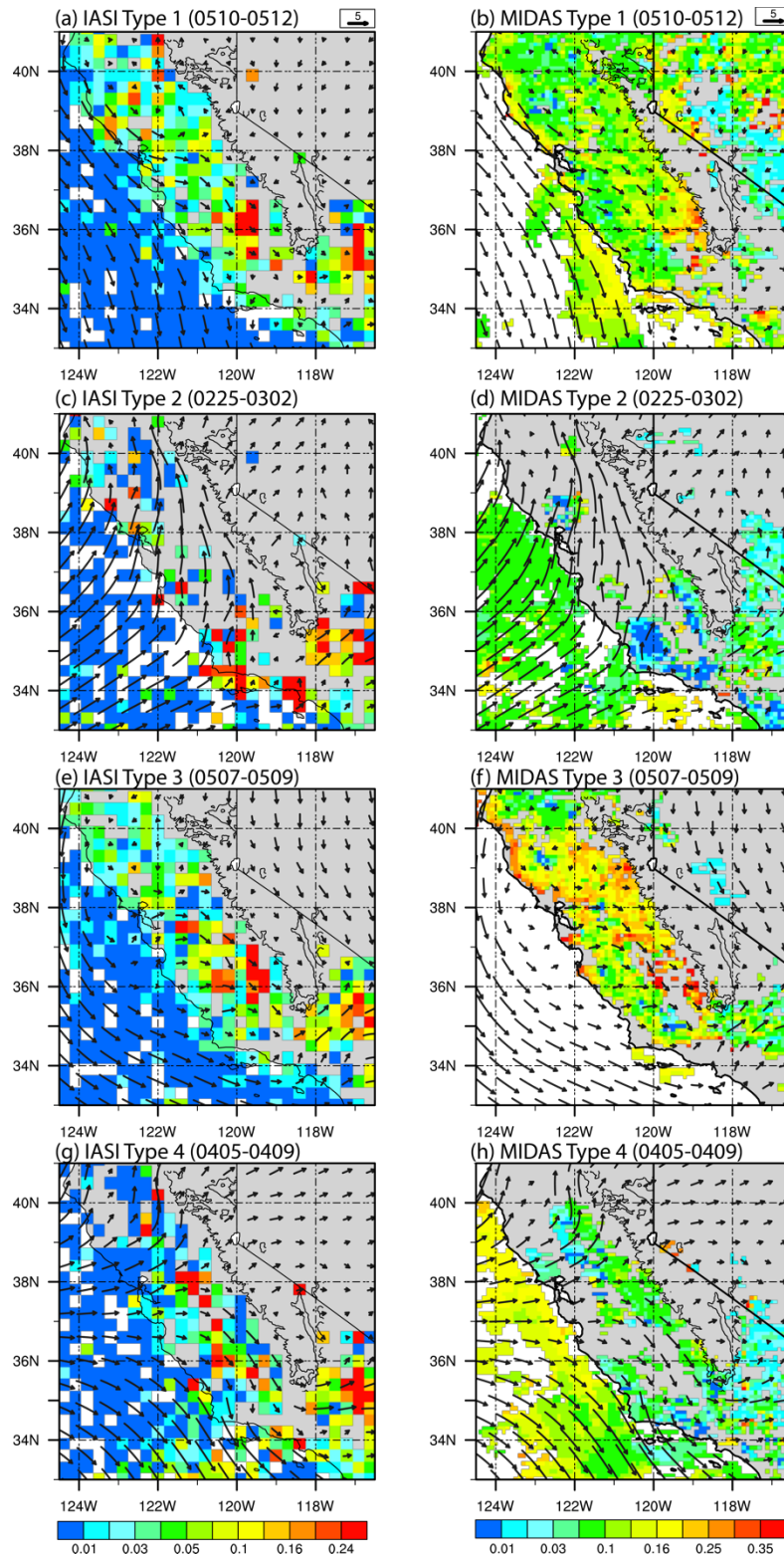
314
315 **Figure 7** (a,c,e,g) IR DOD at the wavelength of 10 μm retrieved from IASI and (b,d,f,h) visible DOD at
316 the wavelength of 550 μm from MIDAS for each type. The low-level winds (vectors; m s^{-1}) are obtained
317 from the ERA5 reanalyses. The numbers in the parenthesis indicate the event time period for the year 2019.
318
319 **3.2.2 Sierra-barrier-jets-related (SBJ-related) transport**

320   In type 2, the low-level winds turn to the north above the western slope of the Sierra Nevada (Fig.

321   3c), which resembles the terrain-locked Sierra barrier jets (SBJs) typically observed during the presence of

322   ARs (Neiman et al., 2013). The large-scale pattern consists of a low 500hPa geopotential height (GPH)

323   center in the north Pacific (Fig. 6b). The meridional gradient produces intense storm tracks from Kuroshio

324   Current towards Alaska (Rodionov et al., 2007). Indeed, we find extensive precipitations in type 2 (not

325   shown), which produce more wet deposition along the mountain's windward (west and south-facing) slopes

326   and result in cleaner air in the Central Valley (Fig. 3c). The dust layer at the Central Valley is found below

327   700 hPa, mostly blocked by the high mountain peaks and is hardly transported to the lee-side (east) slope

328   of the mountain (Fig. 5b), despite the cross-barrier westerlies found in the middle level. Dominated by SBJs,

329   dust generated in the Great Basin and the Mojave Desert is blown away from the mountain. No clear signal

330   of remote transport is found on the California coast (Fig. 3d). The dust transport from all sources is closely

331   connected to SBJ; therefore, type 2 is referred to as the "SBJ-related" transport. In both IASI and MIDAS,

332   we find more missing pixels for SBJ-related transport than any other type caused by cloud contamination

333   (Figs. 7c-d). The AR-related landfalling precipitations from February 25 to March 2 remove the airborne

334   dust particles. A cleaner atmosphere might be induced, but it is hard to confirm considering the missing

335   pixels over the continent.

336   **3.2.3 North-Pacific-High-related (NPH-related) transport**

337   Type 3 has northwestern winds in both Central Valley and the Great Basin (Fig. 3e), transporting

338   Central Valley dust to the southwest part of the Sierra Nevada in early summer. It is known as the "North-

339   Pacific-High-related (NPH-related)" transport, during which the North Pacific High (NPH) built up in the

340   north Pacific 130° W produces the northwest-southeast wind direction along the California coast (Fig. 6c),

341   influencing the transport patterns for dust emitted from the surrounding sources. At the middle level, we

342   observe a meridional mid-level dust transport pathway (Fig. 3f), which appears at 400-500 hPa in the

343   northern Sierra Nevada and descends to 700 hPa at 36-37 °N, the top of the southern Sierra Nevada (Fig.

344   5c). "The MERRA-2 reanalysis DOD (Fig. 6c) further shows dust originating from Asia is transported

345   towards North America following the isobars and wind patterns (discussed further in section 3.2.3). The

346   dust emitted from the Great basin is transported by the southward winds to the east slope of the mountains,

347   while emissions from the Mojave Desert are transported away from the mountain range.

348   The simulated dust concentration and transport in the NPH-related transport are confirmed by DOD

349   observations during May 7-9, with the transport pathway parallel to the California coast (Figs. 7e-f). Studies

350   have shown two main pathways of Asian dust transport to North America during the spring months: (1)

351   meridional excursions north into Alaska and then south along the U.S. west coast, and (2) zonal transport

352   over the North Pacific Ocean (Creamean et al., 2014). With north-south dust transport at the middle level,

353   the NPH-related transport characterizes the first pathway. To examine this hypothesis, we averaged the IR

354   DOD and 500 hPa wind field over the North Pacific during May 2-9. We included a few days before the

355   event (Fig. 8a) as it takes 7-10 days for dust to be transported from Asia to North America (Ault et al., 2011;

356   Creamean et al., 2013). The dust transport pathway shows that after being emitted from East Asia and the

357   Gobi Desert, dust is transported zonally to 150 °W, excursing north into Alaska/Canada and then traveling

358   south along the U.S. west coast. Similar conclusions can be drawn with more evident pathways using DOD

359   from MERRA-2 reanalyses (Fig. 8e). An elevated dust belt from 8 km to 12 km is discerned over the North

360   American coast (27 °N to 60 °N) from the CALIOP data, denoting the north-south transport of a thin dust

361   layer through the middle level (Fig. 8c).
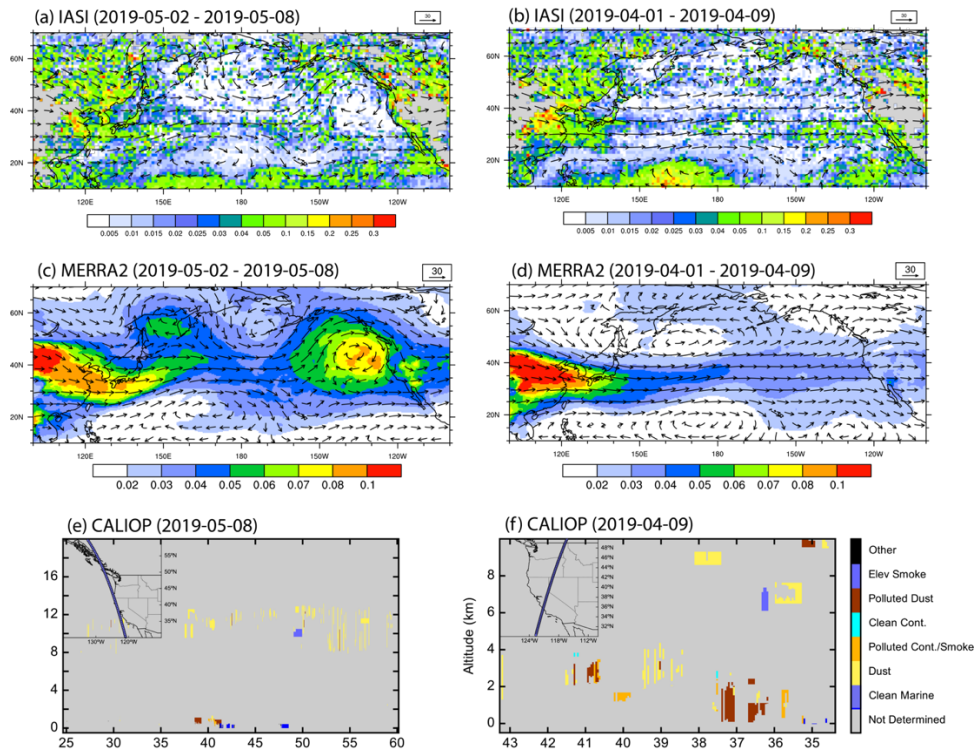
Figure 8 (a) IR DOD from IASI and 500 hPa winds (m s^{-1}) from ERA5 over the North Pacific for a typical Type 3 case averaged between 2019-05-02 to 2019-05-08; (b) same as (a) but for a typical type 4 event averaged between 2019-04-01 to 2019-04-09; (c) DOD from MERRA-2 and 500 hPa winds (m s^{-1}) from ERA5 for a 3 event; (d) same as (c) but for a type 4 event; (e) latitude-height cross-section of aerosol species from CALIOP on 2019-05-08 (Type 3); (f) same as (e) but for a typical Type 4 case on 2019-04-09

3.2.4 Cross-Pacific zonal (CPZ) transport

Air inflows from the ocean enter California and diverge to the northern and southern branches in type 4, transporting dust eastward across the Sierra Nevada (Fig. 3g). At the middle level, the low-GPH center recedes in April, and the isobars become straighter than in boreal winter, which facilitates the zonal transport of dust emitted from middle Asia over the North Pacific Ocean (Fig. 6d). The cross-section further shows an elevated dust layer is transported from the ocean at around 700-500 hPa (Fig. 5d). The concentrations are much stronger, and the altitude also lower than the NPH-related transport (Fig. 5c). The remotely transported dust descends to low altitudes when reaching the California coast and converges with the dust from the Central Valley at around 800 hPa. A portion of dust is compacted to the windward slopes at higher elevations, and the remaining across the mountains affects the east slope. Dust emitted from the

20

379   Great Basin and the Mojave Desert is transported away from the mountains. Type 4 is denoted with "cross-

380   Pacific zonal (CPZ) transport" to reflect the strong cross-Pacific dust transport.

381   April 5-9, a typical case for the CPZ transport, clearly shows the north and south branches of dust

382   transport over the Central Valley (Figs. 7g-h). Different from the NPH-related transport pathway, the large-

383   scale DOD and winds at 500 hPa (averaged over April 1-9) show that dust emitted from East Asia is being

384   transported eastward, with a belt of IR DOD > 0.1 evident around 25-40 °N (Fig. 8b). The DOD from

385   MERRA-2 confirms the zonal pathways of dust transport with a smaller magnitude (Fig. 8d). The vertical

386   distribution shows an elevated dust layer at 2-4 km above ground level, reaching the higher elevation of the

387   mountain (Fig. 8f).

388   We calculated the mid-level dust remote transport, defined as the dust influxes from the north and

389   west boundaries of the 200-700 hPa of WRF-Chem modeling domain 1, and investigated how the top 10%

390   largest remote transport distribute in each SOM (Fig. 4b). Among all the large remote transport, CPZ

391   transport accounts for 48% while NPH-related accounts for 32%, indicating that the zonal pathway plays a

392   more important role in the cross-Pacific transport. Most remote transports are found in April and May, the

393   former dominated by the meridional transport in the existence of the NPH while the latter led by the CPZ

394   transport. The remaining two types contribute to a fairly small portion consistent with the clean atmosphere

395   in the middle levels (Figs. 3b, d).

396

397   **3.2.5 Dust emissions and transport in back trajectory analyses**

398   We discern four types of dust transport patterns across the Sierra Nevada using the SOM clustering

399   method. The MSR transport represents the local dust transport, which contributes to more than 20% of the

400   time each month during February-June (Fig. 4a) in the absence of prevailing weather systems. The SBJ-

401   related air inflows transport dust eastward and are closely related to the AR, during which the GPH and

402   storm tracks at 500 hPa feature a typical large-scale pattern during the boreal winter (Rodionov et al., 2007).

403   As time evolves, the GPH center recedes, and the isobars become more straight zonally in April, bringing

404   dust from Asia and Africa to the western U.S. coast (CPZ transport). In early summer, the buildup of NPH

405   in the east Pacific corresponds to north-south winds along the California coast, transporting dust along the

406   Sierra Nevada (NPH-related transport).

407   We further conducted air mass back trajectory (AMBT) simulations to evaluate the dust emission

408   sources and transport pathways identified using SOM analyses. The back trajectory simulation was

409   conducted using Hybrid Single-Particle Lagrangian Integrated Trajectory (HYSPLIT) model with

410   meteorological forcings from North American Mesoscale Forecast System. We selected typical days for

411   the four SOM types as in Figure 7 and three sites located at the Central Sierra Nevada (38 °N, 120.3°W),

412   Southern Sierra Nevada (36.5 °N, 119 °W), and Eastern Sierra Nevada (37 °N, 117 °W), to represent dust

413   deposition at different subregions.

414   The results of 12-hour and 7-day AMBT results corroborate the identified local and long-range

415   transport pathways for each type. The transport pathways generally follow the wind directions shown in

416   Figure 7. Multiple emission source regions are found in type 1, including the Central Valley where dust is

417   transported eastward to the windward slopes and the Great Basin where dust is transported westward to the

418   lee-side slopes (Fig. S2). In type 2, dust deposited in all three sites comes from the Central Valley (Fig. S2),

419   and the transport corresponds to the direction of SBJ during AR (Fig. 7c). Types 3 and 4 are affected by

420   both local and remote transport. Locally, dDust mainly comes from the northern California and the Great

421   Basin in type 3, while it comes from the Central Valley in type 4. Remotely, in type 3, we find dust emitted

422   from Asia and North Africa excurses meridionally to Alaska at 135° W and then travels southward along

423   the U.S. West Coast (Fig. S3a). In contrast, dust emitted from east Asia is transported zonally across the

424   Pacific, reaching the Sierra Nevada from the west (Fig. S3b).

425   **3.3 Dust deposition over the Sierra Nevada**

426   The averaged dust deposition and low-level dust transport for each type are shown in Fig. 9, including

427   both dry and wet depositions. The dry depositions consider the diffusion and gravitational effects, while

428   wet depositions describe in-cloud removal (rainout) and below-cloud removal (washout) by grid-resolved

429   stratiform precipitation as well as the sub-grid wet scavenging (Chapman et al., 2009; Easter et al., 2004).

430   In all SOM types, extensive depositions are found on the west slope in all types, generally decreasing with

431   elevation.

432   The MSR transport has the smallest deposition among the four types (Fig. 9a). Large depositions are

433   found in the southern Sierra Nevada and Lake Tahoe. Dust contributing to the deposition origins mainly

434   from the Mojave Desert and the Great Basin dryland. In contrast, large depositions found in the southern

435   and eastern parts of the mountains in NPH-related transport may be produced in agricultural land from the

436   southern Central Valley, as we find a persistent eastward transport pathway in the low level (Fig. 9c). The

437   remote transported dust plays a minor role as it is located above 8 km in altitude.
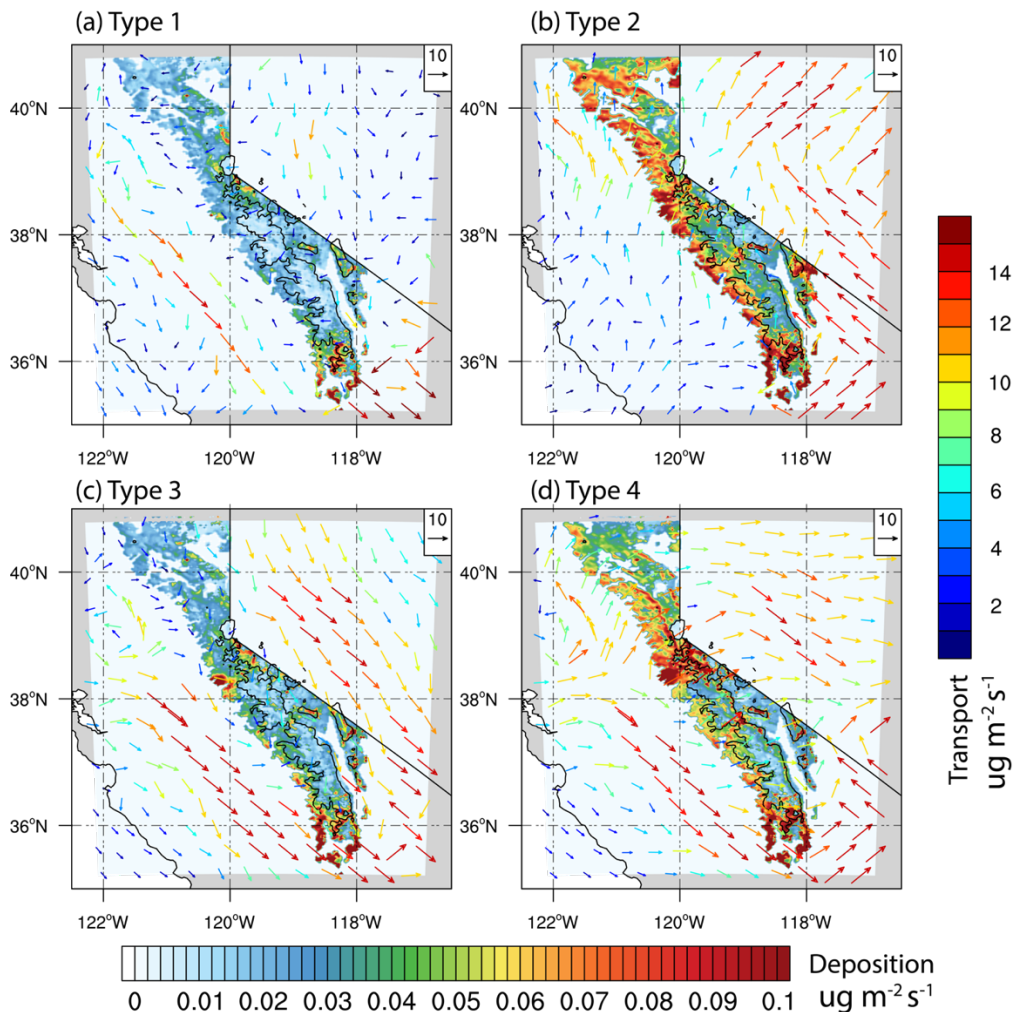
438
439   **Figure 9** (a-d) Dust deposition (shaded; ug m^{-2} s^{-1}) over the Sierra Nevada and low-level dust transport
440   fluxes (colored vectors; ug m^{-2} s^{-1}) across the Sierra Nevada averaged over each of the four SOM types in
441   WRF-Chem. Black contours indicate an elevation of 2500 m. The bottom color bar shows the magnitude
442   of dust deposition over the Sierra Nevada while the right color bar shows the magnitude of dust transport
443   flux vectors.

444

While SBJ-related transport has the lowest low-level dust concentration over the Central Valley, it produces the largest deposition along the west slope (Fig. 9b). Most eastward transport in the southern Sierra Nevada is obstructed by the high mountain peaks, resulting in large depositions below 2900 m. The SBJ turns eastward in the Sacramento Basins and climbs through the mountain north of 38 °N, producing a relatively homogenous deposition in the northern part. The combination of dust transport and deposition indicates that dust influencing the mountain snow impurities mostly comes from the Central Valley. Compared with the other SOM types, SBJ-related transport has large depositions at elevations higher than 2500 m (discuss later). Large depositions are also found in the CPZ transport (Fig. 9d), with the largest value occurring on the west slope of the central and southern Sierra Nevada, contributed by both Asian dust and Central Valley dust. Compared to the MSR and NPH-related transport, the large-scale westerlies in the Central Valley (SBJ-related and cross-Pacific transport) produce larger deposition, probably because of the more efficient removal of particles by collision with terrestrial surfaces at higher elevations (Fig. 5d).

To quantify the relative importance of wet and dry depositions in each 3 hourly total deposition data, we calculate the fraction of wet depositions to total depositions averaged over the Sierra Nevada: $\frac{Wet\ deposition}{Wet\ deposition+Dry\ deposition}$. The contribution of dry deposition is defined in a similar way. We find the wet deposition accounting for 40% in frequency in the SBJ-related type. The landfalling precipitation has deposited large amounts of airborne dust on the snow surface, producing a cleaner atmosphere as we have found in Fig. 3c. The frequent wet depositions also explain the larger depositions in high elevations (Fig. 9b): dust particles reaching the high mountains are small in size and difficult to deposit through gravitational effects. Wet deposition is a more efficient way of depositing small particles as they collect dust in raindrops. In contrast, ~~the~~ dry depositions play predominant roles (more than 80% in frequency) in all the other types (Fig. 10a). Figure 10b further shows the contribution of wet deposition increases with deposition intensity. The averaged contribution of wet depositions in magnitude increases from 19% in all events to 29% in the

top 10 percentile, 36% in the top 5 percentile, and 56% in the top 1 percentile largest events, supporting

our conclusion that wet deposition is a more efficient way of dust deposition.
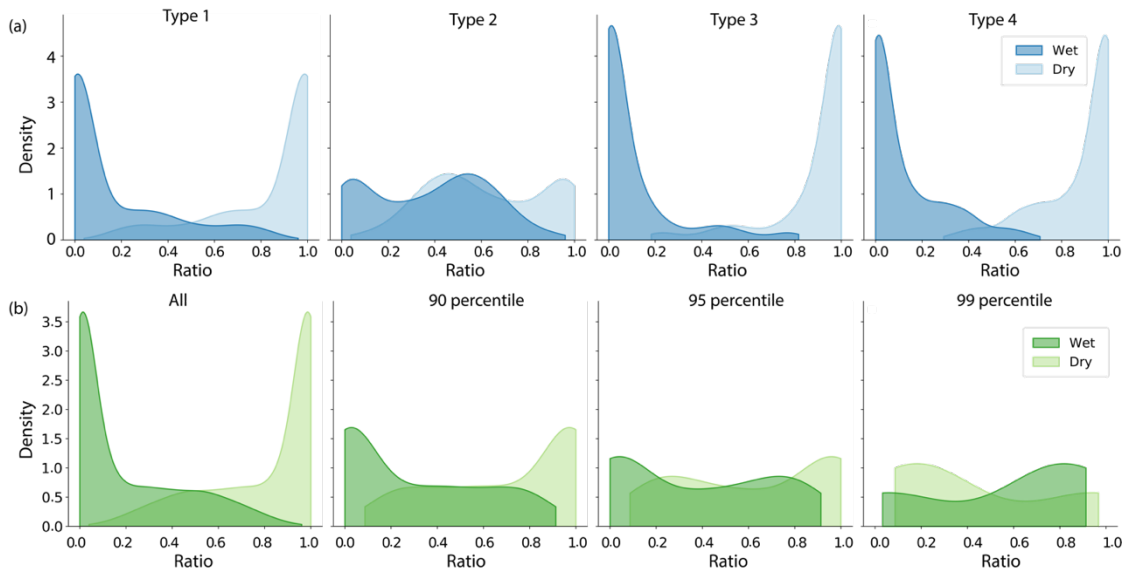
Figure 10 (a) Distribution of contribution of wet and dry depositions to total deposition in each type in WRF-Chem. (b) Distribution of contribution of wet and dry depositions to total deposition for all depositions, depositions over 90th, 95th, and 99th percentile.

3.4 Features of the dust transport in MERRA-2

We repeated the SOM analyses using 2019 MERRA-2 data to examine the WRF-Chem model

performance and interannual variability. We conducted additional SOM analyses using 2001-2021

climatology MERRA-2 data to investigate the interannual variability of the transport patterns. The low-

level and mid-level dust transport features identified in MERRA-2 (Figs. 11-12) are similar to their

corresponding types in WRF-Chem (Fig. 3), with types 1, 2, 3, and 4 representing MSR, SBJ-related, NPH-

related and CPZ transport, respectively (Fig. 11). Additionally, north-south transport occurs in the middle

layer in type 3 and west-east transport in type 4, despite the slight difference in the peak region (Fig. 12).
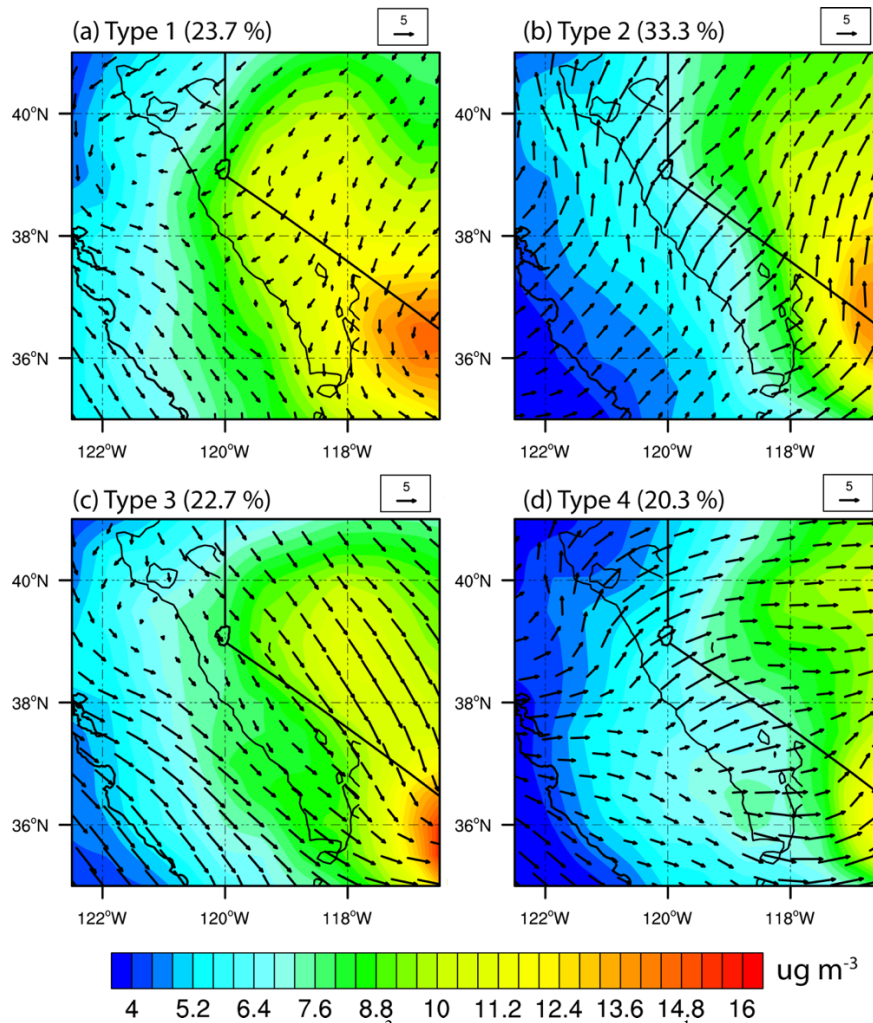
Figure 11 Low-level dust concentration (ug m^{-3}) and wind vectors (m s^{-1}) in each of the four SOM types from MERRA-2 for the year 2019. The numbers on the top of the subplots denote the frequency of each type.
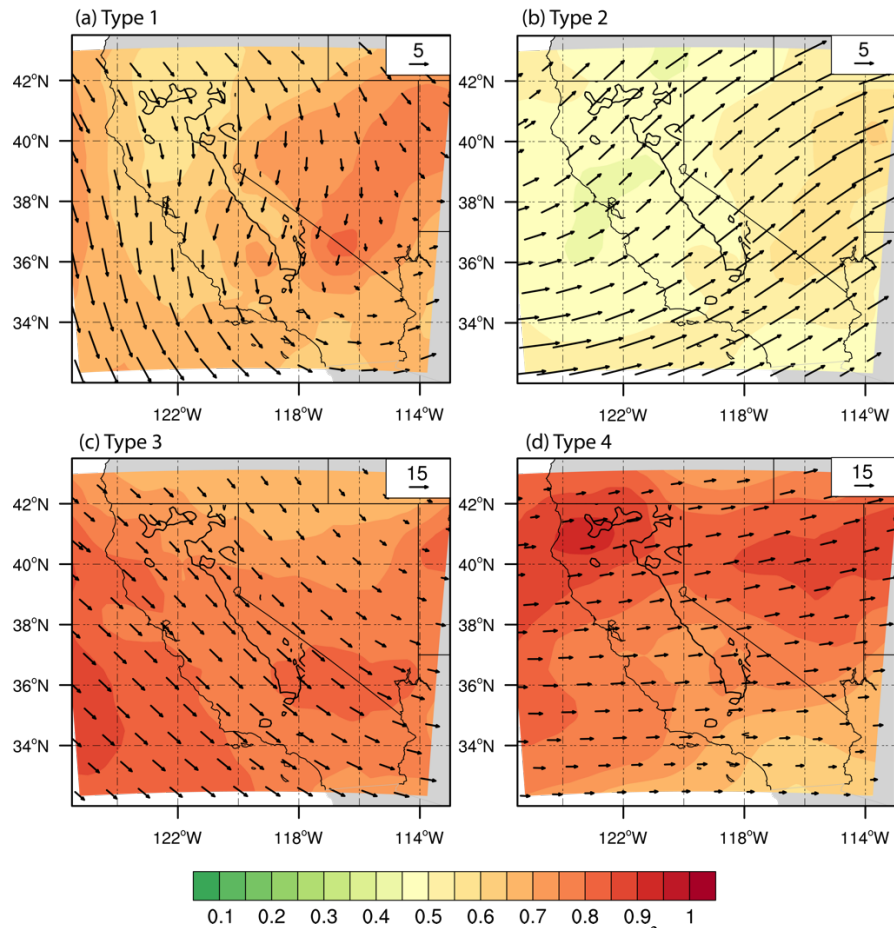
Figure 12 Mid-level (200-700 hPa average) dust concentration (ug m^{-3}) and dust transport fluxes (ug m^{-2} s^{-1}) in each of the four SOM types from MERRA-2 for the year 2019

The relative contribution of each transport type in MERRA-2 (SBJ-related > MSR > CPZ > NPH-related) is generally consistent with the results in WRF-Chem (MSR > SBJ-related > CPZ > NPH-related), except that the MSR transport occurs less frequently in MERRA-2. The difference is largely caused by the spatial resolution of the two datasets. With a resolution of 0.5°×0.625°, MERRA-2 has smooth topography information and cannot resolve the high peaks of the Sierra Nevada which produce the MSR winds and transport. Consequently, MSR transport contributes to a smaller fraction in the MERRA-2. The coarser resolution MERRA-2 also produces a more homogeneous dust concentration at low levels than 2-km WRF-Chem.

Similar dust concentrations and transport patterns are found in the 21-year SOM analysis (Fig. 13), indicating that the four patterns identified in 2019 are representative of the climatological conditions. In

27

501 climatology, the SBJ is weaker and air inflows hit the California coast at a further north latitude (about

502 40 °N; Fig. 13b), which is reasonable as 2019 is an El Niño year with stronger AR reaching California

503 further south than usual.

504   The changes in the transport patterns reflect the interannual variations of large-scale forcings and

505 regional weather conditions, which is investigated using the frequency of each type in a year during 2001-

506 2021 (Fig. S4). Types 1 and 4 have a negative correlation coefficient (R=-0.75) in their frequency,

507 indicating the competing impact between remote transport and local emissions on dust concentrations over

508 the Sierra Nevada. Especially, type 4 tends to occur more frequently during La Niña years while less

509 frequently during El Niño years. An opposite conclusion can be drawn for type 1. We further examine the

510 dust transport pattern and the frequency of the four SOM types during three La Niña (2008, 2011, and 2021)

511 and three El Niño (2015, 2016, and 2019) years. We find that the La Niña years have larger dust

512 concentrations than El Niño years in both lower levels and middle levels (Figs. S5-S8), due to suppressed

513 precipitations and drier soil in the southwestern U.S. Meanwhile, the frequencies of types 3 and 4 are higher

514 in El Niño years, reflecting the increased contribution of cross-Pacific transport to dust loading over

515 California. The increase of remote transport weakens the relative importance of local emissions, decreasing

516 the frequency of type 1.
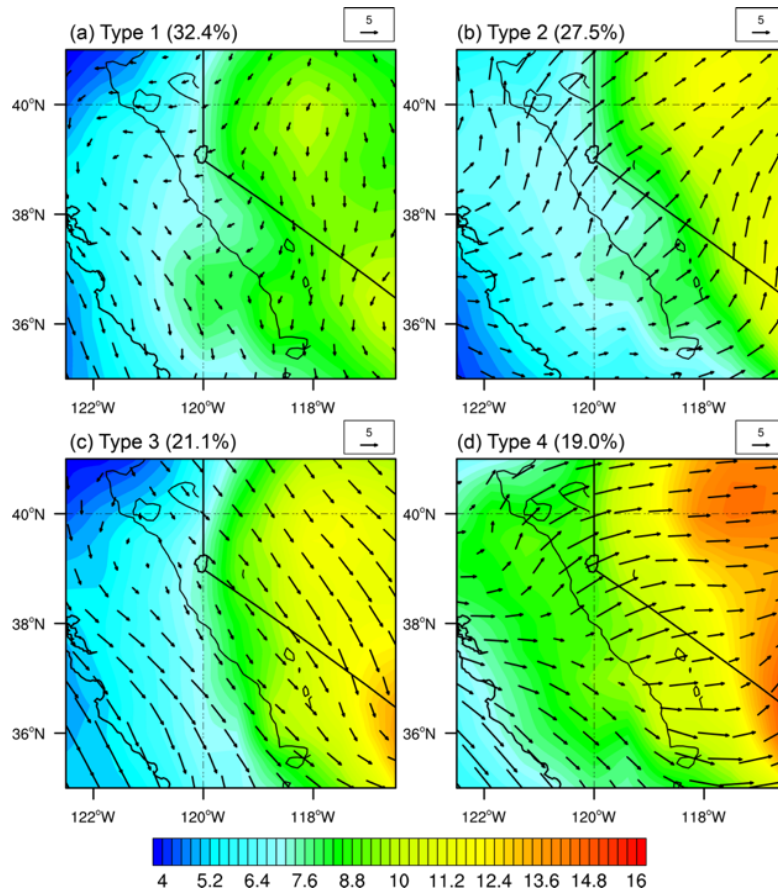
Figure 13 Low level dust concentration (ug m^{-3}) and wind vectors (m s^{-1}) in each of the four SOM types from MERRA-2 averaged over 2001-2021. The numbers on the top right of subplots denote the frequency of each type.

4. Conclusions and discussion

523
524 **Figure 14** Schematic diagram of typical dust transport patterns across the Sierra Nevada. The "MSR"
525 demotes mesoscale regional transport. The "SBJ" and "NPH" denotes dust transport dominated by Sierra-
526 Barrier Jets (SBJ) and North Pacific High (NPH), respectively, while the "CPZ" denotes Cross-Pacific
527 Zonal transport.
528

529　　　　With a focus on the dust that influences ~~the~~ mountain snow, we investigated the dust sources

530　surrounding the Sierra Nevada and their typical transport patterns during the spring and early summer.

531　Despite the strongest emissions from the Mojave Desert, dust is only transported northward to the mountain

532　when the mesoscale weather pattern dominates the southwest U.S. (Fig. 14). During 64.25% of our study

533　period, dust from the Mojave Desert is transported away from the mountains. Dust emitted from the Great

534　Basin is transported to the central Sierra Nevada during MSR transport and to the eastern part when the

535　NPH builds in the eastern Pacific. It is blown eastward by air inflows from the ocean during SBJ or cross-

536　Pacific transport. In contrast, dust produced by the Central Valley is persistently transported to the west

537 mountain slope, playing an essential role in snow impurities there. Carried by intense air inflows, it can be

538 transported to the lee-side of the Sierra Nevada.

539 During April, Asia dust is transported zonally over the North Pacific through the straight zonal

540 isobars at the middle level. The dust layer descends to 800 hPa when it reaches the California coast. In the

541 presence of the NPH, dust emitted from Asia excurses north into Alaska/Canada and travels south along

542 the U.S. west coast. The dust travels at a higher altitude, and the concentrations are weaker than the zonal

543 transport.

544 Large amounts of depositions are found on the west slope, which generally decrease with elevations.

545 Dust particles transported to the higher altitude are small in size and difficult to deposit through gravitational

546 effects. The SBJ-produced AR collects dust in the rain and snow and deposits it on the high mountain.

547 Besides, considerable depositions occur when the elevated dust layer from the Pacific collides with the

548 mountain.We acknowledge that our characterization of dominant transport patterns might be limited by

549 model uncertainties. Besides, the coarse-resolution reanalyses data, MERRA-2, cannot accurately resolve

550 the topography effects and tends to underestimate mesoscale regional transport. Furthermore, both WRF-

551 Chem and MERRA-2 describe dust emissions from dryland by relating them to high wind speed, soil

552 moisture, and soil type (Ginoux et al., 2001), while dust emission from agricultural lands is not specifically

553 implemented. However, a comprehensive evaluation of airborne dust and PM2.5 concentration between

554 model simulation and site observations in our previous study shows a good agreement between both (Huang

555 et al., 2022a). In addition, the dust transport pathways have well-defined patterns associated with the

556 mesoscale and large-scale weather systems. The general consistency across different models (WRF-Chem

557 and MERRA-2) and observations (satellite analysis) and across different years also give us confidence that

558 the results are valid despite model uncertainties.

559 The analyses of dust emissions and transport can be used to understand dust transport in a changing

560 climate. Studies have shown that global warming continues to dry the soil, producing more dust emissions

561 over the western U.S. Nevertheless, the change in transport and deposition patterns has not been well

562 recognized. Our study highlighted the connection between dust transport and dominant weather patterns

563   across the Sierra Nevada; the latter might respond in a more predictable way to climate change. Future

564   projections show that global warming may increase the frequency of landfalling AR by 20-35% by the end

565   of the 21st century (Hagos et al., 2016; Rhoades et al., 2021). Besides, the widening of the Hadley Cell in

566   response to global warming might enhance the NPH and shift it poleward (Song et al., 2018; Choi et al.,

567   2016). Thus said, the SBJ- and NPH-related dust transport may occur more frequently while the MSR

568   transport may become less common. In this regard, changes in dust emissions from the Central Valley might

569   play a more critical role in mountain snow impurities than those from the Mojave Desert and the Great

570   Basin, producing more depositions on the west slope of the Sierra Nevada.

571

572   **Data availability:**

573   The IASI DOD data is acquired from https://iasi.aeris-data.fr/dust-aod/. The MIDAS DOD is acquired from

574   https://zenodo.org/record/4244106#.YsJqe-zMIws. MERRA-2 aerosol reanalyses are available from

575   https://disc.gsfc.nasa.gov/datasets?keywords=MERRA2&page=1 and ERA5 wind reanalyses are available

576   from https://rda.ucar.edu/datasets/ds633.0/. The WRF-Chem and MERRA-2 SOM clustering results have

577   been uploaded to https://doi.org/10.5281/zenodo.6795994.

578

579   **Author contributions:**

580   HH performed the analysis and drafted the manuscript. The methodology was developed by HH and YL.

581   JZ and AG provided the observational data used for model validation. YQ, CH, and ZZ helped with the

582   analysis and offered valuable comments. All authors contributed to writing and editing the manuscript.

583

584   **Competing interests:**

585   The authors declare that they have no conflict of interest.

586

587   **Acknowledgement:**

594 Reference:

595 Aarons, S. M., Arvin, L. J., Aciego, S. M., Riebe, C. S., Johnson, K. R., Blakowski, M. A., Koornneef,
596 J. M., Hart, S. C., Barnes, M. E., Dove, N., Botthoff, J. K., Maltz, M., and Aronson, E. L.: Competing
597 droughts affect dust delivery to Sierra Nevada, Aeolian Research, 41, 100545,
598 https://doi.org/10.1016/j.aeolia.2019.100545, 2019.
599 Achakulwisut, P., Shen, L., and Mickley, L. J.: What Controls Springtime Fine Dust Variability in the
600 Western United States? Investigating the 2002–2015 Increase in Fine Dust in the U.S. Southwest,
601 Journal of Geophysical Research: Atmospheres, 122, 12,449-412,467,
602 https://doi.org/10.1002/2017JD027208, 2017.
603 Aciego, S. M., Riebe, C. S., Hart, S. C., Blakowski, M. A., Carey, C. J., Aarons, S. M., Dove, N. C.,
604 Botthoff, J. K., Sims, K. W. W., and Aronson, E. L.: Dust outpaces bedrock in nutrient supply to
605 montane forest ecosystems, Nat Commun, 8, 14800, 10.1038/ncomms14800, 2017.
606 Ault, A. P., Williams, C. R., White, A. B., Neiman, P. J., Creamean, J. M., Gaston, C. J., Ralph, F. M.,
607 and Prather, K. A.: Detection of Asian dust in California orographic precipitation, Journal of
608 Geophysical Research: Atmospheres, 116, https://doi.org/10.1029/2010JD015351, 2011.
609 Bao, J.-W., Michelson, S. A., Persson, P. O. G., Djalalova, I. V., and Wilczak, J. M.: Observed and
610 WRF-Simulated Low-Level Winds in a High-Ozone Episode during the Central California Ozone
611 Study, Journal of Applied Meteorology and Climatology, 47, 2372-2394,
612 10.1175/2008jamc1822.1, 2008.
613 Bao, M. and Wallace, J. M.: Cluster Analysis of Northern Hemisphere Wintertime 500-hPa Flow
614 Regimes during 1920–2014, J Atmos Sci, 72, 3597-3608, 10.1175/JAS-D-15-0001.1, 2015.
615 Brahney, J., Ballantyne, A. P., Sievers, C., and Neff, J. C.: Increasing Ca2+ deposition in the western
616 US: The role of mineral aerosols, Aeolian Research, 10, 77-87,
617 https://doi.org/10.1016/j.aeolia.2013.04.003, 2013.
618 Buchard, V., da Silva, A. M., Randles, C. A., Colarco, P., Ferrare, R., Hair, J., Hostetler, C., Tackett,
619 J., and Winker, D.: Evaluation of the surface PM2.5 in Version 1 of the NASA MERRA Aerosol
620 Reanalysis over the United States, Atmos Environ, 125, 100-111,
621 https://doi.org/10.1016/j.atmosenv.2015.11.004, 2016.
622 Buchard, V., Randles, C. A., da Silva, A. M., Darmenov, A., Colarco, P. R., Govindaraju, R., Ferrare,
623 R., Hair, J., Beyersdorf, A. J., Ziemba, L. D., and Yu, H.: The MERRA-2 Aerosol Reanalysis, 1980
624 Onward. Part II: Evaluation and Case Studies, J Climate, 30, 6851-6872, 10.1175/JCLI-D-16-0613.1,
625 2017.
626 Buchholz, R., Emmons, L., and Tilmes, S.: CESM2. 1/CAM-chem instantaneous output for
627 boundary conditions, in: UCAR/NCAR-Atmospheric Chemistry Observations and Modeling
628 Laboratory, 2019.
629 Capelle, V., Chédin, A., Pondrom, M., Crevoisier, C., Armante, R., Crepeau, L., and Scott, N. A.:
630 Infrared dust aerosol optical depth retrieved daily from IASI and comparison with AERONET over
631 the period 2007–2016, Remote Sens Environ, 206, 15-32,
632 https://doi.org/10.1016/j.rse.2017.12.008, 2018.
633 Capelle, V., Chédin, A., Siméon, M., Tsamalis, C., Pierangelo, C., Pondrom, M., Crevoisier, C.,
634 Crepeau, L., and Scott, N. A.: Evaluation of IASI-derived dust aerosol characteristics over the
635 tropical belt, Atmos. Chem. Phys., 14, 9343-9362, 10.5194/acp-14-9343-2014, 2014.

Chapman, E. G., Gustafson, W. I., Easter, R. C., Barnard, J. C., Ghan, S. J., Pekour, M. S., and Fast, J. D.: Coupling aerosol-cloud-radiative processes in the WRF-Chem model: Investigating the radiative impact of elevated point sources, Atmos Chem Phys, 9, 945-964, 10.5194/acp-9-945-2009, 2009.

Chin, M., Diehl, T., Ginoux, P., and Malm, W.: Intercontinental transport of pollution and dust aerosols: implications for regional air quality, Atmos. Chem. Phys., 7, 5501-5517, 10.5194/acp-7-5501-2007, 2007.

Chin, M., Ginoux, P., Kinne, S., Torres, O., Holben, B. N., Duncan, B. N., Martin, R. V., Logan, J. A., Higurashi, A., and Nakajima, T.: Tropospheric Aerosol Optical Thickness from the GOCART Model and Comparisons with Satellite and Sun Photometer Measurements, J Atmos Sci, 59, 461-483, 10.1175/1520-0469(2002)059<0461:Taotft>2.0.Co;2, 2002.

Choi, J., Lu, J., Son, S. W., Frierson, D. M., and Yoon, J. H.: Uncertainty in future projections of the North Pacific subtropical high and its implication for California winter precipitation change, Journal of Geophysical Research: Atmospheres, 121, 795-806, 2016.

Clausnitzer, H. and Singer, M. J.: Environmental influences on respirable dust production from agricultural operations in California, Atmos Environ, 34, 1739-1745, https://doi.org/10.1016/S1352-2310(99)00385-4, 2000.

Creamean, J. M., Spackman, J. R., Davis, S. M., and White, A. B.: Climatology of long-range transported Asian dust along the West Coast of the United States, Journal of Geophysical Research: Atmospheres, 119, 12,171-112,185, https://doi.org/10.1002/2014JD021694, 2014.

Creamean, J. M., Suski, K. J., Rosenfeld, D., Cazorla, A., DeMott, P. J., Sullivan, R. C., White, A. B., Ralph, F. M., Minnis, P., and Comstock, J. M.: Dust and biological aerosols from the Sahara and Asia influence precipitation in the western US, Science, 339, 1572-1578, 2013.

Crooks, J. L., Cascio, W. E., Percy, M. S., Reyes, J., Neas, L. M., and Hilborn, E. D.: The Association between Dust Storms and Daily Non-Accidental Mortality in the United States, 1993–2005, Environ Health Persp, 124, 1735-1743, doi:10.1289/EHP216, 2016.

Duniway, M. C., Pfennigwerth, A. A., Fick, S. E., Nauman, T. W., Belnap, J., and Barger, N. N.: Wind erosion and dust from US drylands: a review of causes, consequences, and solutions in a changing world, Ecosphere, 10, e02650, https://doi.org/10.1002/ecs2.2650, 2019.

Easter, R. C., Ghan, S. J., Zhang, Y., Saylor, R. D., Chapman, E. G., Laulainen, N. S., Abdul-Razzak, H., Leung, L. R., Bian, X. D., and Zaveri, R. A.: MIRAGE: Model description and evaluation of aerosols and trace gases, J Geophys Res-Atmos, 109, Artn D20210
10.1029/2004jd004571, 2004.

Emmons, L. K., Schwantes, R. H., Orlando, J. J., Tyndall, G., Kinnison, D., Lamarque, J. F., Marsh, D., Mills, M. J., Tilmes, S., Bardeen, C., Buchholz, R. R., Conley, A., Gettelman, A., Garcia, R., Simpson, I., Blake, D. R., Meinardi, S., and Petron, G.: The Chemistry Mechanism in the Community Earth System Model Version 2 (CESM2), J Adv Model Earth Sy, 12, e2019MS001882, ARTN e2019MS001882
10.1029/2019MS001882, 2020.

Forster, P., Ramaswamy, V., Artaxo, P., Berntsen, T., Betts, R., Fahey, D. W., Haywood, J., Lean, J., Lowe, D. C., and Myhre, G.: Changes in atmospheric constituents and in radiative forcing. Chapter 2, in: Climate change 2007. The physical science basis, 2007.

Gelaro, R., McCarty, W., Suarez, M. J., Todling, R., Molod, A., Takacs, L., Randles, C., Darmenov, A., Bosilovich, M. G., Reichle, R., Wargan, K., Coy, L., Cullather, R., Draper, C., Akella, S., Buchard,

680 V., Conaty, A., da Silva, A., Gu, W., Kim, G. K., Koster, R., Lucchesi, R., Merkova, D., Nielsen, J. E.,
681 Partyka, G., Pawson, S., Putman, W., Rienecker, M., Schubert, S. D., Sienkiewicz, M., and Zhao, B.:
682 The Modern-Era Retrospective Analysis for Research and Applications, Version 2 (MERRA-2), J
683 Clim, Volume 30, 5419-5454, 10.1175/JCLI-D-16-0758.1, 2017.
684 Giannadaki, D., Pozzer, A., and Lelieveld, J.: Modeled global effects of airborne desert dust on air
685 quality and premature mortality, Atmos Chem Phys, 14, 957-968, 2014.
686 Ginoux, P., Prospero, J. M., Gill, T. E., Hsu, N. C., and Zhao, M.: Global-scale attribution of
687 anthropogenic and natural dust sources and their emission rates based on MODIS Deep Blue
688 aerosol products, Reviews of Geophysics, 50, https://doi.org/10.1029/2012RG000388, 2012.
689 Ginoux, P., Chin, M., Tegen, I., Prospero, J. M., Holben, B., Dubovik, O., and Lin, S. J.: Sources and
690 distributions of dust aerosols simulated with the GOCART model, J Geophys Res-Atmos, 106,
691 20255-20273, Doi 10.1029/2000jd000053, 2001.
692 Gkikas, A., Proestakis, E., Amiridis, V., Kazadzis, S., Di Tomaso, E., Marinou, E., Hatzianastassiou,
693 N., Kok, J. F., and García-Pando, C. P.: Quantification of the dust optical depth across
694 spatiotemporal scales with the MIDAS global dataset (2003–2017), Atmos. Chem. Phys., 22, 3553-
695 3578, 10.5194/acp-22-3553-2022, 2022.
696 Gkikas, A., Proestakis, E., Amiridis, V., Kazadzis, S., Di Tomaso, E., Tsekeri, A., Marinou, E.,
697 Hatzianastassiou, N., and Pérez García-Pando, C.: ModIs Dust AeroSol (MIDAS): a global fine-
698 resolution dust optical depth data set, Atmos. Meas. Tech., 14, 309-334, 10.5194/amt-14-309-
699 2021, 2021.
700 Goldstein, H. L., Breit, G. N., and Reynolds, R. L.: Controls on the chemical composition of saline
701 surface crusts and emitted dust from a wet playa in the Mojave Desert (USA), J Arid Environ, 140,
702 50-66, https://doi.org/10.1016/j.jaridenv.2017.01.010, 2017.
703 Hagos, S. M., Leung, L. R., Yoon, J.-H., Lu, J., and Gao, Y.: A projection of changes in landfalling
704 atmospheric river frequency and extreme precipitation over western North America from the
705 Large Ensemble CESM simulations, Geophys Res Lett, 43, 1357-1363,
706 https://doi.org/10.1002/2015GL067392, 2016.
707 Hand, J. L., Gill, T. E., and Schichtel, B. A.: Spatial and seasonal variability in fine mineral dust and
708 coarse aerosol mass at remote sites across the United States, Journal of Geophysical Research:
709 Atmospheres, 122, 3080-3097, https://doi.org/10.1002/2016JD026290, 2017.
710 Hand, J. L., White, W. H., Gebhart, K. A., Hyslop, N. P., Gill, T. E., and Schichtel, B. A.: Earlier onset
711 of the spring fine dust season in the southwestern United States, Geophys Res Lett, 43, 4001-
712 4009, https://doi.org/10.1002/2016GL068519, 2016.
713 Hannachi, A.: On the origin of planetary-scale extratropical winter circulation regimes, J Atmos
714 Sci, 67, 1382-1401, 2010.
715 Haywood, J. M., Allan, R. P., Culverwell, I., Slingo, T., Milton, S., Edwards, J., and Clerbaux, N.: Can
716 desert dust explain the outgoing longwave radiation anomaly over the Sahara during July 2003?,
717 Journal of Geophysical Research: Atmospheres, 110, https://doi.org/10.1029/2004JD005232,
718 2005.
719 Hersbach, H., Bell, B., Berrisford, P., Hirahara, S., Horanyi, A., Munoz-Sabater, J., Nicolas, J.,
720 Peubey, C., Radu, R., Schepers, D., Simmons, A., Soci, C., Abdalla, S., Abellan, X., Balsamo, G.,
721 Bechtold, P., Biavati, G., Bidlot, J., Bonavita, M., De Chiara, G., Dahlgren, P., Dee, D., Diamantakis,
722 M., Dragani, R., Flemming, J., Forbes, R., Fuentes, M., Geer, A., Haimberger, L., Healy, S., Hogan,
723 R. J., Holm, E., Janiskova, M., Keeley, S., Laloyaux, P., Lopez, P., Lupu, C., Radnoti, G., de Rosnay,

724   P., Rozum, I., Vamborg, F., Villaume, S., and Thepaut, J. N.: The ERA5 global reanalysis, Q J Roy
725   Meteor Soc, 146, 1999-2049, 10.1002/qj.3803, 2020.
726   Hilton, F., Armante, R., August, T., Barnet, C., Bouchard, A., Camy-Peyret, C., Capelle, V., Clarisse,
727   L., Clerbaux, C., Coheur, P. F., Collard, A., Crevoisier, C., Dufour, G., Edwards, D., Faijan, F., Fourrie,
728   N., Gambacorta, A., Goldberg, M., Guidard, V., Hurtmans, D., Illingworth, S., Jacquinet-Husson,
729   N., Kerzenmacher, T., Klaes, D., Lavanant, L., Masiello, G., Matricardi, M., McNally, A., Newman,
730   S., Pavelin, E., Payan, S., Pequignot, E., Peyridieu, S., Phulpin, T., Remedios, J., Schlussel, P., Serio,
731   C., Strow, L., Stubenrauch, C., Taylor, J., Tobin, D., Wolf, W., and Zhou, D.: HYPERSPECTRAL EARTH
732   OBSERVATION FROM IASI Five Years of Accomplishments, B Am Meteorol Soc, 93, 347-370,
733   10.1175/Bams-D-11-00027.1, 2012.
734   Huang, H., Gu, Y., Xue, Y., Jiang, J., and Zhao, B.: Assessing aerosol indirect effect on clouds and
735   regional climate of East/South Asia and West Africa using NCEP GFS, Clim Dyn, 52, 5759-5774,
736   10.1007/s00382-018-4476-9, 2019.
737   Huang, H., Qian, Y., He, C., Bair, E. H., and Rittger, K.: Snow Albedo Feedbacks Enhance Snow
738   Impurity-Induced Radiative Forcing in the Sierra Nevada, Geophys Res Lett, 49, e2022GL098102,
739   https://doi.org/10.1029/2022GL098102, 2022a.
740   Huang, H., Fischella, M. R., Liu, Y., Ban, Z., Fayne, J. V., Li, D., Cavanaugh, K. C., and Lettenmaier,
741   D. P.: Changes in Mechanisms and Characteristics of Western U.S. Floods Over the Last Sixty Years,
742   Geophys Res Lett, 49, e2021GL097022, 10.1029/2021gl097022, 2022b.
743   Hunt, W. H., Winker, D. M., Vaughan, M. A., Powell, K. A., Lucker, P. L., and Weimer, C.: CALIPSO
744   Lidar Description and Performance Assessment, Journal of Atmospheric and Oceanic Technology,
745   26, 1214-1228, 10.1175/2009jtecha1223.1, 2009.
746   Jardine, G. E., Crocker, A. J., Bailey, I., Cooper, M. J., Milton, J. A., and Wilson, P. A.: The imprint
747   of windblown dust from the North American Southwest on the California Channel Islands and
748   Pacific Ocean sediments, Quaternary Science Reviews, 261, 106934,
749   https://doi.org/10.1016/j.quascirev.2021.106934, 2021.
750   Kim, D., Chin, M., Cruz, C. A., Tong, D., and Yu, H.: Spring Dust in Western North America and Its
751   Interannual Variability—Understanding the Role of Local and Transported Dust, Journal of
752   Geophysical Research: Atmospheres, 126, e2021JD035383,
753   https://doi.org/10.1029/2021JD035383, 2021.
754   Kim, M. H., Omar, A. H., Tackett, J. L., Vaughan, M. A., Winker, D. M., Trepte, C. R., Hu, Y., Liu, Z.,
755   Poole, L. R., Pitts, M. C., Kar, J., and Magill, B. E.: The CALIPSO version 4 automated aerosol
756   classification and lidar ratio selection algorithm, Atmos. Meas. Tech., 11, 6107-6135,
757   10.5194/amt-11-6107-2018, 2018.
758   Laden, F., Schwartz, J., Speizer, F. E., and Dockery, D. W.: Reduction in fine particulate air pollution
759   and mortality: Extended follow-up of the Harvard Six Cities study, Am J Respir Crit Care Med, 173,
760   667-672, 10.1164/rccm.200503-443OC, 2006.
761   Lei, H. and Wang, J. X. L.: Observed characteristics of dust storm events over the western United
762   States using meteorological, satellite, and air quality measurements, Atmos. Chem. Phys., 14,
763   7847-7857, 10.5194/acp-14-7847-2014, 2014.
764   Lim, S. S., Vos, T., Flaxman, A. D., Danaei, G., Shibuya, K., Adair-Rohani, H., AlMazroa, M. A.,
765   Amann, M., Anderson, H. R., Andrews, K. G., Aryee, M., Atkinson, C., Bacchus, L. J., Bahalim, A.
766   N., Balakrishnan, K., Balmes, J., Barker-Collo, S., Baxter, A., Bell, M. L., Blore, J. D., Blyth, F., Bonner,
767   C., Borges, G., Bourne, R., Boussinesq, M., Brauer, M., Brooks, P., Bruce, N. G., Brunekreef, B.,

Bryan-Hancock, C., Bucello, C., Buchbinder, R., Bull, F., Burnett, R. T., Byers, T. E., Calabria, B., Carapetis, J., Carnahan, E., Chafe, Z., Charlson, F., Chen, H., Chen, J. S., Cheng, A. T.-A., Child, J. C., Cohen, A., Colson, K. E., Cowie, B. C., Darby, S., Darling, S., Davis, A., Degenhardt, L., Dentener, F., Des Jarlais, D. C., Devries, K., Dherani, M., Ding, E. L., Dorsey, E. R., Driscoll, T., Edmond, K., Ali, S. E., Engell, R. E., Erwin, P. J., Fahimi, S., Falder, G., Farzadfar, F., Ferrari, A., Finucane, M. M., Flaxman, S., Fowkes, F. G. R., Freedman, G., Freeman, M. K., Gakidou, E., Ghosh, S., Giovannucci, E., Gmel, G., Graham, K., Grainger, R., Grant, B., Gunnell, D., Gutierrez, H. R., Hall, W., Hoek, H. W., Hogan, A., Hosgood, H. D., Hoy, D., Hu, H., Hubbell, B. J., Hutchings, S. J., Ibeanusi, S. E., Jacklyn, G. L., Jasrasaria, R., Jonas, J. B., Kan, H., Kanis, J. A., Kassebaum, N., Kawakami, N., Khang, Y.-H., Khatibzadeh, S., Khoo, J.-P., Kok, C., Laden, F., Lalloo, R., Lan, Q., Lathlean, T., Leasher, J. L., Leigh, J., Li, Y., Lin, J. K., Lipshultz, S. E., London, S., Lozano, R., Lu, Y., Mak, J., Malekzadeh, R., Mallinger, L., Marcenes, W., March, L., Marks, R., Martin, R., McGale, P., McGrath, J., Mehta, S., Memish, Z. A., Mensah, G. A., Merriman, T. R., Micha, R., Michaud, C., Mishra, V., Hanafiah, K. M., Mokdad, A. A., Morawska, L., Mozaffarian, D., Murphy, T., Naghavi, M., Neal, B., Nelson, P. K., Nolla, J. M., Norman, R., Olives, C., Omer, S. B., Orchard, J., Osborne, R., Ostro, B., Page, A., Pandey, K. D., Parry, C. D. H., Passmore, E., Patra, J., Pearce, N., Pelizzari, P. M., Petzold, M., Phillips, M. R., Pope, D., Pope, C. A., Powles, J., Rao, M., Razavi, H., Rehfuess, E. A., Rehm, J. T., Ritz, B., Rivara, F. P., Roberts, T., Robinson, C., Rodriguez-Portales, J. A., Romieu, I., Room, R., Rosenfeld, L. C., Roy, A., Rushton, L., Salomon, J. A., Sampson, U., Sanchez-Riera, L., Sanman, E., Sapkota, A., Seedat, S., Shi, P., Shield, K., Shivakoti, R., Singh, G. M., Sleet, D. A., Smith, E., Smith, K. R., Stapelberg, N. J. C., Steenland, K., Stöckl, H., Stovner, L. J., Straif, K., Straney, L., Thurston, G. D., Tran, J. H., Van Dingenen, R., van Donkelaar, A., Veerman, J. L., Vijayakumar, L., Weintraub, R., Weissman, M. M., White, R. A., Whiteford, H., Wiersma, S. T., Wilkinson, J. D., Williams, H. C., Williams, W., Wilson, N., Woolf, A. D., Yip, P., Zielinski, J. M., Lopez, A. D., Murray, C. J. L., and Ezzati, M.: A comparative risk assessment of burden of disease and injury attributable to 67 risk factors and risk factor clusters in 21 regions, 1990–2010: a systematic analysis for the Global Burden of Disease Study 2010, The Lancet, 380, 2224-2260, https://doi.org/10.1016/S0140-6736(12)61766-8, 2012.

Liu, Y., Qian, Y., and Berg, L. K.: Local-thermal-gradient and large-scale-circulation impacts on turbine-height wind speed forecasting over the Columbia River Basin, Wind Energ. Sci., 7, 37-51, 10.5194/wes-7-37-2022, 2022a.

Liu, Y., Qian, Y., Feng, S., Berg, L. K., Juliano, T. W., Jiménez, P. A., and Liu, Y.: Sensitivity of solar irradiance to model parameters in cloud and aerosol treatments of WRF-solar, Solar Energy, 233, 446-460, 2022b.

Muhs, D. R., Budahn, J., Reheis, M., Beann, J., Skipp, G., and Fisher, E.: Airborne dust transport to the eastern Pacific Ocean off southern California: Evidence from San Clemente Island, Journal of Geophysical Research: Atmospheres, 112, https://doi.org/10.1029/2006JD007577, 2007.

Neff, J. C., Ballantyne, A. P., Farmer, G. L., Mahowald, N. M., Conroy, J. L., Landry, C. C., Overpeck, J. T., Painter, T. H., Lawrence, C. R., and Reynolds, R. L.: Increasing eolian dust deposition in the western United States linked to human activity, Nat Geosci, 1, 189-195, 10.1038/ngeo133, 2008.

Neiman, P. J., Hughes, M., Moore, B. J., Ralph, F. M., and Sukovich, E. M.: Sierra Barrier Jets, Atmospheric Rivers, and Precipitation Characteristics in Northern California: A Composite Perspective Based on a Network of Wind Profilers, Mon Weather Rev, 141, 4211-4233, 10.1175/mwr-d-13-00112.1, 2013.

Okin, G., Gillette, D., and Herrick, J.: Multi-scale controls on and consequences of aeolian processes in landscape change in arid and semi-arid environments, J Arid Environ, 65, 253-275, 2006.

Pappagianis, D. and Einstein, H.: Tempest from Tehachapi takes toll or Coccidioides conveyed aloft and afar, Western Journal of Medicine, 129, 527, 1978.

Pu, B. and Ginoux, P.: How reliable are CMIP5 models in simulating dust optical depth?, Atmos. Chem. Phys., 18, 12491-12510, 10.5194/acp-18-12491-2018, 2018.

Qian, Y., Gustafson, W. I., Leung, L. R., and Ghan, S. J.: Effects of soot-induced snow albedo change on snowpack and hydrological cycle in western United States based on Weather Research and Forecasting chemistry and regional climate simulations, J Geophys Res-Atmos, 114, Artn D03108 10.1029/2008jd011039, 2009.

Qian, Y., Yasunari, T. J., Doherty, S. J., Flanner, M. G., Lau, W. K. M., Ming, J., Wang, H., Wang, M., Warren, S. G., and Zhang, R.: Light-absorbing particles in snow and ice: Measurement and modeling of climatic and hydrological impact, Adv Atmos Sci, 32, 64-91, 10.1007/s00376-014-0010-0, 2014.

Randles, C. A., Da Silva, A. M., Buchard, V., Colarco, P. R., Darmenov, A., Govindaraju, R., Smirnov, A., Holben, B., Ferrare, R., Hair, J., Shinozuka, Y., and Flynn, C. J.: The MERRA-2 Aerosol Reanalysis, 1980 - onward, Part I: System Description and Data Assimilation Evaluation, J Clim, 30, 6823-6850, 10.1175/JCLI-D-16-0609.1, 2017.

Reheis, M. C. and Kihl, R.: Dust Deposition in Southern Nevada and California, 1984-1989 - Relations to Climate, Source Area, and Source Lithology, J Geophys Res-Atmos, 100, 8893-8918, Doi 10.1029/94jd03245, 1995.

Reusch, D. B., Alley, R. B., and Hewitson, B. C.: North Atlantic climate variability from a self-organizing map perspective, Journal of Geophysical Research: Atmospheres, 112, https://doi.org/10.1029/2006JD007460, 2007.

Rhoades, A. M., Risser, M. D., Stone, D. A., Wehner, M. F., and Jones, A. D.: Implications of warming on western United States landfalling atmospheric rivers and their flood damages, Weather Clim Extreme, 32, 100326, https://doi.org/10.1016/j.wace.2021.100326, 2021.

Rodionov, S. N., Bond, N. A., and Overland, J. E.: The Aleutian Low, storm tracks, and winter climate variability in the Bering Sea, Deep Sea Research Part II: Topical Studies in Oceanography, 54, 2560-2577, https://doi.org/10.1016/j.dsr2.2007.08.002, 2007.

Sarangi, C., Qian, Y., Rittger, K., Leung, L. R., Chand, D., Bormann, K. J., and Painter, T. H.: Dust dominates high-altitude snow darkening and melt over high-mountain Asia, Nat Clim Change, 10, 1045-+, 10.1038/s41558-020-00909-3, 2020.

Skiles, S. M., Flanner, M., Cook, J. M., Dumont, M., and Painter, T. H.: Radiative forcing by light-absorbing particles in snow, Nat Clim Change, 8, 964-971, 10.1038/s41558-018-0296-5, 2018.

Song, F., Leung, L. R., Lu, J., and Dong, L.: Future Changes in Seasonality of the North Pacific and North Atlantic Subtropical Highs, Geophys Res Lett, 45, 11,959-911,968, https://doi.org/10.1029/2018GL079940, 2018.

Song, F., Feng, Z., Leung, L. R., Houze Jr, R. A., Wang, J., Hardin, J., and Homeyer, C. R.: Contrasting Spring and Summer Large-Scale Environments Associated with Mesoscale Convective Systems over the U.S. Great Plains, J Climate, 32, 6749-6767, 10.1175/JCLI-D-18-0839.1, 2019.

854 Song, Q., Zhang, Z., Yu, H., Ginoux, P., and Shen, J.: Global dust optical depth climatology derived
855 from CALIOP and MODIS aerosol retrievals on decadal timescales: regional and interannual
856 variability, Atmos. Chem. Phys., 21, 13369-13395, 10.5194/acp-21-13369-2021, 2021.
857 Tong, D. Q., Wang, J. X. L., Gill, T. E., Lei, H., and Wang, B.: Intensified dust storm activity and
858 Valley fever infection in the southwestern United States, Geophys Res Lett, 44, 4304-4312,
859 https://doi.org/10.1002/2017GL073524, 2017.
860 Vicars, W. C. and Sickman, J. O.: Mineral dust transport to the Sierra Nevada, California: Loading
861 rates and potential source areas, J Geophys Res-Biogeo, 116, Artn G01018
862 10.1029/2010jg001394, 2011.
863 Vigaud, N. and Robertson, A. W.: Convection regimes and tropical‐midlatitude interactions over
864 the Intra‐American Seas from May to November, Int J Climatol, 37, 987-1000, 2017.
865 Vigaud, N., Robertson, A. W., and Tippett, M. K.: Predictability of recurrent weather regimes over
866 North America during winter from submonthly reforecasts, Mon Weather Rev, 146, 2559-2577,
867 2018.
868 Visbeck, M. H., Hurrell, J. W., Polvani, L., and Cullen, H. M.: The North Atlantic Oscillation: past,
869 present, and future, Proceedings of the National Academy of Sciences, 98, 12876-12877, 2001.
870 von Storch, H., Langenberg, H., and Feser, F.: A spectral nudging technique for dynamical
871 downscaling purposes, Mon Weather Rev, 128, 3664-3673, 2000.
872 Voss, K. K. and Evan, A. T.: A New Satellite-Based Global Climatology of Dust Aerosol Optical
873 Depth, Journal of Applied Meteorology and Climatology, 59, 83-102, 10.1175/JAMC-D-19-0194.1,
874 2020.
875 Voss, K. K., Evan, A. T., and Ralph, F. M.: Evaluating the Meteorological Conditions Associated
876 With Dusty Atmospheric Rivers, Journal of Geophysical Research: Atmospheres, 126,
877 e2021JD035403, https://doi.org/10.1029/2021JD035403, 2021.
878 Winker, D. M., Vaughan, M. A., Omar, A., Hu, Y. X., Powell, K. A., Liu, Z. Y., Hunt, W. H., and Young,
879 S. A.: Overview of the CALIPSO Mission and CALIOP Data Processing Algorithms, Journal of
880 Atmospheric and Oceanic Technology, 26, 2310-2323, 10.1175/2009jtecha1281.1, 2009.
881 Winker, D. M., Pelon, J., Coakley, J. A., Ackerman, S. A., Charlson, R. J., Colarco, P. R., Flamant, P.,
882 Fu, Q., Hoff, R. M., Kittaka, C., Kubar, T. L., Le Treut, H., McCormick, M. P., Megie, G., Poole, L.,
883 Powell, K., Trepte, C., Vaughan, M. A., and Wielicki, B. A.: THE CALIPSO MISSION A Global 3D View
884 of Aerosols and Clouds, B Am Meteorol Soc, 91, 1211-1229, 10.1175/2010bams3009.1, 2010.
885 Wu, L. T., Su, H., Kalashnikova, O. V., Jiang, J. H., Zhao, C., Garay, M. J., Campbell, J. R., and Yu, N.
886 P.: WRF-Chem simulation of aerosol seasonal variability in the San Joaquin Valley, Atmos Chem
887 Phys, 17, 7291-7309, 10.5194/acp-17-7291-2017, 2017.
888 Wu, L. T., Gu, Y., Jiang, J. H., Su, H., Yu, N. P., Zhao, C., Qian, Y., Zhao, B., Liou, K. N., and Choi, Y.
889 S.: Impacts of aerosols on seasonal precipitation and snowpack in California based on convection-
890 permitting WRF-Chem simulations, Atmos Chem Phys, 18, 5529-5547, 10.5194/acp-18-5529-
891 2018, 2018.
892 Young, S. A., Vaughan, M. A., Garnier, A., Tackett, J. L., Lambeth, J. D., and Powell, K. A.: Extinction
893 and optical depth retrievals for CALIPSO's Version 4 data release, Atmospheric Measurement
894 Techniques, 11, 5701-5727, 10.5194/amt-11-5701-2018, 2018.
895 Yu, H., Tan, Q., Chin, M., Remer, L. A., Kahn, R. A., Bian, H., Kim, D., Zhang, Z., Yuan, T., Omar, A.
896 H., Winker, D. M., Levy, R. C., Kalashnikova, O., Crepeau, L., Capelle, V., and Chédin, A.: Estimates
897 of African Dust Deposition Along the Trans-Atlantic Transit Using the Decadelong Record of

898   Aerosol Measurements from CALIOP, MODIS, MISR, and IASI, Journal of Geophysical Research:
899   Atmospheres, 124, 7975-7996, https://doi.org/10.1029/2019JD030574, 2019.
900   Zaveri, R. A. and Peters, L. K.: A new lumped structure photochemical mechanism for large-scale
901   applications, Journal of Geophysical Research: Atmospheres, 104, 30387-30415, 1999.
902   Zheng, J., Zhang, Z., Garnier, A., Yu, H., Song, Q., Wang, C., Dubuisson, P., and Di Biagio, C.: The
903   thermal infrared optical depth of mineral dust retrieved from integrated CALIOP and IIR
904   observations, Remote Sens Environ, 270, 112841, https://doi.org/10.1016/j.rse.2021.112841,
905   2022.
906